PHYSICAL REVIEW E **107**, 015103 (2023)

Impact of interfacial rheology on finger tip splitting

Habakuk Conrado,[*] Eduardo O. Dias,[†] and José A. Miranda[‡]
Departamento de Física, Universidade Federal de Pernambuco, Recife, Pernambuco 50670-901 Brazil

(Received 10 October 2022; accepted 22 December 2022; published 17 January 2023)

Fluid-fluid interfaces, laden with polymers, surfactants, lipid bilayers, proteins, solid particles, or other surface-active agents, often exhibit a rheologically complex response to deformations. Despite its academic and practical relevance to fluid dynamics and various other fields of research, the role of interfacial rheology in viscous fingering remains fairly underexplored. A noteworthy exception is the work by Li and Manikantan [Phys. Rev. Fluids **6**, 074001 (2021)], who used linear stability analysis to show that surface rheological stresses act to stabilize the development of radial viscous fingering at the linear regime. In this paper, we perform a perturbative, second-order mode-coupling analysis of the system and investigate the influence of interfacial rheology on the morphology of the fingering structures at early nonlinear stages of the dynamics. In particular, we focus on understanding how interfacial rheology impacts the emblematic finger tip-widening and finger tip-splitting phenomena that take place in radial viscous fingering in Hele-Shaw cells. We describe the viscous Newtonian fluid-fluid interface by using a Boussinesq-Scriven model, and derive a generalized Young-Laplace pressure jump condition at the fluid-fluid interface. In this framing, we go beyond the purely linear description and use Darcy's law to obtain a perturbative mode-coupling differential equation which describes the time evolution of the perturbation amplitudes, accurate to second order. Our early nonlinear mode-coupling results indicate that regardless of their stabilizing action at the linear regime, interfacial rheology effects favor finger tip widening, leading to the occurrence of enhanced finger tip-splitting events.

DOI: 10.1103/PhysRevE.107.015103

I. INTRODUCTION

When a less viscous fluid displaces a more viscous one in the narrow passage between two close parallel plates of a Hele-Shaw cell, the fluid-fluid interface becomes unstable, leading to the phenomenon of viscous fingering [1]. In a classical work, Saffman and Taylor [2] studied the viscous fingering problem in a rectangular Hele-Shaw cell (longitudinal flow in a rectangular channel) where air invades glycerine. In such a rectangular geometry, pressure is applied at one of the edges of the channel, pushing a fluid against the other. As a result, the initially flat interface separating the fluids is destabilized by a pressure gradient and the interface deforms, developing small lobes growing in the form of "fingers" [3–6]. For the typical high viscosity contrast situation studied by Saffman and Taylor, fingered structures compete dynamically, eventually leading to the formation of a single, round-tipped, steady-state finger.

A different pattern-forming scenario arises when the flow takes place in a radial Hele-Shaw cell setup [7–11], where the less viscous fluid is injected under constant injection rate at the center of the cell and drives radially the more viscous fluid. Under these axisymmetric constant fluid injection conditions, the initial fluid-fluid interface is circular, until the front becomes deformed, and a few small fingerlike protrusions arise. As these fingers continue to grow, they widen increasingly and destabilize in the front part of the structures in such a way that their tips split into two parts. This tip-doubling process characterizes the so-called tip-splitting phenomenon. As the split fingers keep advancing, both secondary branches will also become progressively wider until they destabilize again, ultimately forming highly ramified, complex treelike patterns. In contrast to the rectangular Hele-Shaw flow case, this traditional radial displacement presents multiple stages of instability, with no true steady state attainable. In addition, unlike the rectangular geometry situation, in which the single finger normally does not split at its tip, the radial Hele-Shaw flow geometry is markedly characterized by the occurrence of nonlinear finger tip-splitting events.

Since the seminal work by Saffman and Taylor [2], the viscous fingering instability has been the object of extensive studies due to its connection to a variety of natural phenomena and industrial processes, with prominent examples in enhanced oil recovery [12], flow in porous media [13], carbon sequestration [14], and many others [1]. As a matter of fact, over the past 60 years, the viscous fingering (or Saffman-Taylor) problem has become an archetype for studying interfacial instabilities occurring in other related moving boundary problems, including dendrite solidification [15], fluid mixing [16], microdischarges in plasmas [17], and biodynamics of cell fragmentation [18], just to mention a few.

Over the years, investigators have analyzed the effects of a large number of variations of the traditional radial viscous fingering problem. Among many other interesting modifications, theoretical and experimental studies have incorporated

---

[*] cefalo.moreira@ufpe.br
[†] eduardo.dias@ufpe.br
[‡] jose.mirandant@ufpe.br

the presence of non-Newtonian [19,20], miscible [21–23], and reactive [24,25] fluids, the effect of magnetic [26,27] and electric [28,29] fields, time-dependent injection rates [30–34], suspended particles [35,36], the influence of centrifugal and Coriolis forces [37,38], the impact of wetting effects [39,40] and fluid inertia [41–43], as well as the consideration of fluid displacements in geometrically modified Hele-Shaw cells [44–49]. Most of these studies focused on two central points: (i) Try to understand how these various changes influence the morphology and nonlinear dynamics of the pattern-forming structures and (ii) examine possible ways to control, suppress, or enhance the development of fingering patterns, in particular, the growth of finger tip splitting.

Very recently, Li and Manikantan [50] examined a topic that has been considerably underappreciated in the viscous fingering literature: the impact of interfacial rheology stresses on the radial Saffman-Taylor problem. Although it is well-known that, in general, surface-active agents (for instance, polymers, surfactants, lipid bilayers, proteins, and solid particles) act to stabilize interfaces against rupture and coalescence in a number of industrial and natural processes [51–59], a quantitative description of the influence of interfacial rheology in confined radial Hele-Shaw cell flows was indeed lacking. In such types of systems [50–59], the in-plane friction that appears when the molecules or particles within the interface slide past each other produces viscous dissipation (or interfacial viscosities), leading to complex interfacial rheology.

In Ref. [50], Li and Manikantan used a Boussinesq-Scriven model [60–62] and described the fluid-fluid interface as a two-dimensional, compressible Newtonian fluid with intrinsic surface shear and dilatational viscosities. By looking only at small deformations from a uniformly radial sourcelike flow, they considered the simplest possible flow setup in which the unit normal vector pointed only in the radial direction to the interface. By assuming that the vector velocity is predominantly in the radial direction and that the radial velocity component needs be continuous at the interface, they derived a Young-Laplace boundary condition for the problem. This boundary condition expresses the normal stress balance at the interface and takes into account the action of interfacial rheology effects.

By performing a linear stability analysis, Li and Manikantan [50] indicate that at the linear regime, interfacial rheology effects tend to stabilize the radial viscous fingering instability. Physically, one has that the normal flow stretches or dilates the fluid-fluid interface, which in turn is resisted by the interfacial viscosity. Their linear results show the slowing down of the growth rate of the instability for larger interfacial rheology effects, suggesting that the emerging fingers would get thicker as a result of the action of such surface rheological stresses.

Despite the useful information and significant advances obtained in Ref. [50] about the role of interfacial rheology effects on the linear stability of the fluid-fluid interface in radial viscous fingering, their purely linear perturbation theory does not allow one to investigate how the intrinsically nonlinear finger tip-splitting phenomenon is influenced by surface rheological effects. However, it is well-known that a nonlinear perturbative mode-coupling theory permits the prediction and capture of key morphological elements in many interfacial pattern formation problems [1,6,9,63–68]. Motivated by the stimulating linear stability results obtained in Ref. [50], in this paper we employ a perturbative, second-order mode-coupling analysis to examine how interfacial rheology stresses affect the emblematic tip-splitting events in radial Hele-Shaw cells. Our current weakly nonlinear study complements the linear investigation carried out in Ref. [50], and extends it to early nonlinear stages of the flow.

In this paper, our main task is to use a perturbative approach to derive a differential equation for the interfacial perturbations amplitudes using Fourier analysis, but going beyond the level of linear stability analysis in which the Fourier modes do not couple, and focusing on second-order contributions. In addition to going up until second order, and by taking into account the perturbed (noncircular) shape of the evolving fluid-fluid interface, we derive a modified version of the Young-Laplace boundary condition originally calculated in Ref. [50] [their Eq. (10)]. We generalized it by adding two important modifications: First, we consider that the unit normal vector at the perturbed interface may point in an arbitrary direction, having both radial and azimuthal components. On top of this, as a consequence of considering a generic normal vector, we assume a flow setup more general than the one considered in Ref. [50] and propose that the velocity of the two-dimensional fluid that describes the interface is approximately the average of the inner and outer fluid velocities evaluated at the interface. Then, we use Darcy's law to derive an equation of motion for the fluid-fluid interface, including the effects of interfacial rheology. Such a nonlinear differential equation is utilized to investigate how surface rheological stresses impact the development of finger tip-splitting events. Our theoretical results show that, despite their stabilizing nature at the linear regime, surface rheological stresses induce an enhanced growth of finger tip splitting at initial nonlinear stages of the dynamics.

It should be noted that the theoretical studies reported in Ref. [50] and in this paper are not just merely academic, but have connections with some real applications involving the development of interfacial instabilities in the presence of surface-active elements. One emblematic example is oil recovery [12]. It is well-known that viscous fingering is a major factor in reducing oil recovery from underground petroleum reservoirs. On the other hand, it is also known that crude oil is a complex mixture of different compounds, being constituted of hydrocarbons, asphaltenes, resins, traces of metals, etc. [56]. These structures are interfacially active and can strongly couple to hydrodynamic forces, being capable of altering the stability of oil-in-water or water-in-oil emulsions [54]. Thus, it is of scientific and technological importance to understand how to control the growth of patterns under the presence of such rheologically complex interfaces during oil extraction. Other interesting examples are linked to the investigation of pattern-forming interfaces in certain biological systems, such as living cells and biofilms [69–71], where a range of problems relate interfacial rheology, dynamics, and structure. These practical and interdisciplinary examples add to the potential impact of the theoretical analyses performed here and in Ref. [50]. For additional fluid mechanical, soft matter, and

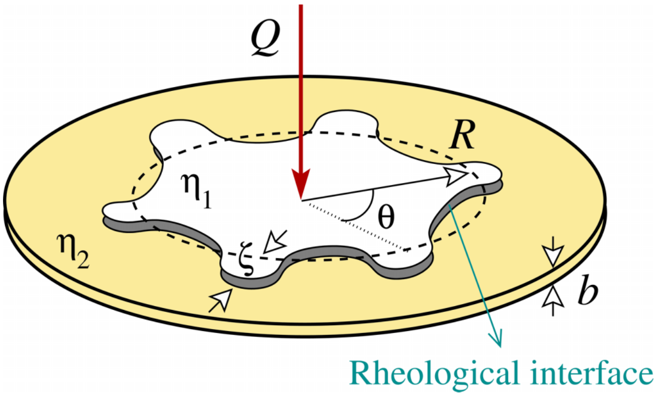

FIG. 1. A schematic of the radial viscous fingering problem in a Hele-Shaw cell of gap thickness b. The inner (outer) fluid has viscosity η_1 (η_2). The fluids are separated by a structured, rheological interface. Fluid 1 is injected into the cell, previously filled with fluid 2, with constant injection rate Q. The time-dependent unperturbed, circular interface (dashed circle) has radius $R(t)$, and the interface perturbation is denoted by $\zeta(\theta, t)$, where θ is the azimuthal angle. The deformed interface is represented as $\mathcal{R}(\theta, t) = R(t) + \zeta(\theta, t)$. The rheological interface has surface tension γ, surface shear viscosity η_s, and dilatational viscosity κ_s.

biomedical systems, and more details about possible targeted processes involving instabilities in structured interfaces, we refer the reader to Refs. [55,59], and references therein.

II. GOVERNING EQUATIONS AND THE SECOND-ORDER MODE-COUPLING DYNAMICS

We split our theoretical formulation into two subsections. In Sec. II A, we present the governing equations for two-fluid flows in a Hele-Shaw cell, considering the influence of interfacial rheology. In Sec. II B, as discussed in the Introduction, to capture the influence of interfacial rheology on the tip-splitting mechanism, we extend the linear stability analysis of Ref. [50] by deriving a second-order, mode-coupling differential equation for the time evolution of the interface perturbation.

A. Governing equations for Hele-Shaw flows with interfacial rheology effects

We consider a radial Hele-Shaw cell of constant gap spacing b containing two immiscible, incompressible, and Newtonian viscous fluids (Fig. 1). The viscosities of the inner fluid (fluid 1) and the outer one (fluid 2) are denoted as η_1 and η_2, respectively. To describe the rheological interface between fluids 1 and 2, we adopt the Boussinesq-Scriven model [50,59–62], where the interface is a continuous isotropic, and compressible, two-dimensional Newtonian fluid with surface tension γ. In addition, excess viscous stresses within the interface are described by two intrinsic surface viscosities, surface shear viscosity η_s, and dilatational viscosity κ_s. These interfacial viscosities result from the in-plane friction that arises when the surface-active entities (molecules, particles, etc.) within the interface slide past each other. In this context, η_s expresses resistance against stretching deformation, while κ_s results when the interface resists expansion and compression. It is worth mentioning that while the apparent surface dilatational viscosity might arise due to finite adsorption or desorption time [50,72], the intrinsic surface dilatational viscosity κ_s is a property of the surface-active agent. Besides, η_s and κ_s are, respectively, the two-dimensional version of the fluid viscosity and dilatational viscosity that appear in the constitutive relation between stress and strain rate [Eq. (7)].

In this setup, fluid 1 is injected at the center of the Hele-Shaw cell at a constant injection rate Q (area covered per unit time), displacing fluid 2, which initially fills the region between the Hele-Shaw plates. During this injection process, the viscosity difference-driven Saffman-Taylor instability induces deformations of the initially circular fluid-fluid interface. In this scenario, the ultimate goal of Secs. II A and II B is to derive a nonlinear differential equation for the evolution of these interface perturbations.

We begin the presentation of the governing equations by introducing the gap-averaged Darcy's law [1,2],

$$\mathbf{u}_j = -\frac{b^2}{12\eta_j}\nabla p_j, \tag{1}$$

which describes the effectively two-dimensional Hele-Shaw flow, and the incompressibility condition for the bulk fluids,

$$\nabla \cdot \mathbf{u}_j = 0, \tag{2}$$

where the index j is 1 for the displacing fluid and 2 for the displaced one. In Eqs. (1) and (2), $\mathbf{u}_j = \mathbf{u}_j(r, \theta)$ and $p_j = p_j(r, \theta)$ denote the gap-averaged velocity and pressure field of fluid $j = 1, 2$, respectively. Here (r, θ) are the usual polar coordinates centered at the injection point, where θ represents the azimuthal angle. By inspecting Eq. (1), one readily verifies the irrotational nature of the flow ($\nabla \times \mathbf{u}_j = 0$) so one can define a velocity potential ϕ_j, where $\mathbf{u}_j = -\nabla\phi_j$. From Eq. (2) and the definition of ϕ_j, one can see that the velocity potentials obey Laplace's equation:

$$\nabla^2\phi_j = 0. \tag{3}$$

We proceed by describing the perturbed interface between fluids 1 and 2 as $r = \mathcal{R}(\theta, t)$. To obtain the equation of motion for $\mathcal{R} = \mathcal{R}(\theta, t)$, first we rewrite Eq. (1) in terms of ϕ_j. Then, we subtract the resulting expression for $j = 1$ from the one for $j = 2$, with both equations evaluated at $r = \mathcal{R}$, and divide by the sum of the two fluids' viscosities. This computation results in the dynamic equation for $\mathcal{R}$ given by

$$A\left(\frac{\phi_1 + \phi_2}{2}\right)_{\mathcal{R}} - \left(\frac{\phi_1 - \phi_2}{2}\right)_{\mathcal{R}} = -\frac{b^2(p_1 - p_2)_{\mathcal{R}}}{12(\eta_1 + \eta_2)}, \tag{4}$$

where $A = (\eta_2 - \eta_1)/(\eta_2 + \eta_1)$ is the viscosity contrast. By examining Eq. (4), we verify that we need to relate both the velocity potentials $\phi_j|_{\mathcal{R}}$, as well as the pressure jump across the interface $(p_1 - p_2)|_{\mathcal{R}}$ with the interfacial perturbations. The former is obtained from Eq. (3) together with the kinematic boundary condition [1], which connects the velocity of the fluids with the motion of the interface itself:

$$\frac{\partial \mathcal{R}}{\partial t} = \left(\frac{1}{r^2}\frac{\partial r}{\partial \theta}\frac{\partial \phi_j}{\partial \theta} - \frac{\partial \phi_j}{\partial r}\right)_{\mathcal{R}}. \tag{5}$$

Equation (5) manifests the fact that the normal components of the fluids' velocities are continuous across the interface.

To determine the pressure jump in Eq. (4), we will follow similar steps to those of Ref. [50]. It is worth mentioning that the interfacial rheology affects the interface dynamic Eq. (4) only through $(p_1 - p_2)_{\mathcal{R}}$. We begin by describing the two-dimensional Cauchy's momentum conservation equation at the interface [73,74],

$$\rho_s \frac{D\mathbf{u}}{Dt} = \mathbf{n} \cdot (\boldsymbol{\sigma}_2 - \boldsymbol{\sigma}_1) + \nabla_s \cdot \boldsymbol{\sigma}_s, \tag{6}$$

where D/Dt is the material derivative, $\mathbf{u}$ is the fluid velocity at the interface, ρ_s is the surface mass density, $\mathbf{n}$ is the unit normal vector pointing towards the outer fluid, and $\boldsymbol{\sigma}_2 - \boldsymbol{\sigma}_1$ is the hydrodynamic stress jump across the interface. Also, $\nabla_s = \mathbf{I}_s \cdot \nabla$ is the surface gradient operator, with $\mathbf{I}_s = \mathbf{I} - \mathbf{nn}$ being the surface identity tensor. In Appendix A, we show some useful identities involving ∇ and ∇_s in polar coordinates. Equation (6) is the two-dimensional analog of the volumetric conservation equation for the momentum. It expresses the condition of the momentum balance at every point on the dividing interface. In this equation, the surface Reynolds transport theorem is used to obtain the term on the left-hand side. On the other hand, the first contribution on the right-hand side (RHS) is a consequence of the contact with the bulk fluids. Finally, the last term is equivalent to the divergence of the stress tensor in a three-dimensional media, representing the internal forces within the interface. Thus, $\boldsymbol{\sigma}_s$ is the stress tensor on the interface, which is given by [55,61]

$$\boldsymbol{\sigma}_s = \gamma \mathbf{I}_s + \boldsymbol{\tau}_{\rm rheo}, \tag{7}$$

where $\boldsymbol{\tau}_{\rm rheo}$ quantifies the deviatoric relationship between stresses and strain rates on the interface.

To obtain $(p_1 - p_2)|_{\mathcal{R}}$ from Cauchy's momentum conservation, first we substitute Eq. (7) into (6), and take the normal component of the resulting expression, yielding

$$\rho_s \frac{D\mathbf{u}}{Dt} \cdot \mathbf{n} - \mathbf{n} \cdot (\boldsymbol{\sigma}_2 - \boldsymbol{\sigma}_1) \cdot \mathbf{n} = \nabla_s \gamma \cdot \mathbf{n} - \gamma(\nabla_s \cdot \mathbf{n}) + (\nabla_s \cdot \boldsymbol{\tau}_{\rm rheo}) \cdot \mathbf{n}. \tag{8}$$

The constitutive relation given by Scriven's generalization of the two-dimensional, compressible Newtonian approximation proposed by Boussinesq [55,61] defines the surface stress tensor $\boldsymbol{\tau}_{\rm rheo}$ as

$$\boldsymbol{\tau}_{\rm rheo} = [(\kappa_s - \eta_s)\nabla_s \cdot \mathbf{u}]\mathbf{I}_s + \eta_s[\nabla_s \mathbf{u} \cdot \mathbf{I}_s + \mathbf{I}_s \cdot (\nabla_s \mathbf{u})^T], \tag{9}$$

where the superscript T denotes a matrix transpose. Note that for highly viscous fluids confined in the geometry of the Hele-Shaw cell, the Reynolds number is significantly low [1], and hence one can safely neglect the contribution of the fluid and surface-active agent inertia $\rho_s D\mathbf{u}/Dt$ in Eq. (8). Besides, as explained in detail in Ref. [50], we make the typical assumption that surface tension is spatially uniform, so the Marangoni stress $\nabla_s \gamma$ vanishes. Under these circumstances and substituting Eq. (9) into Eq. (8), we obtain an expression for the normal stress jump across the interface:

$$\mathbf{n} \cdot (\boldsymbol{\sigma}_1 - \boldsymbol{\sigma}_2) \cdot \mathbf{n} = -\gamma(\nabla_s \cdot \mathbf{n}) - (\kappa_s - \eta_s)(\nabla_s \cdot \mathbf{u})(\nabla_s \cdot \mathbf{n}) + \nabla_s \cdot \{\eta_s[\nabla_s \mathbf{u} \cdot \mathbf{I}_s + \mathbf{I}_s \cdot (\nabla_s \mathbf{u})^T]\} \cdot \mathbf{n}. \tag{10}$$

At this point, it is worth mentioning that in the framework of the Boussinesq-Scriven model [60–62] employed here and in Ref. [50], although the bulk fluids are incompressible [Eq. (2)], the fluid-fluid interface is modelled as a compressible fluid (i.e., $\nabla_s \cdot \mathbf{u} \neq 0$) having viscosities κ_s and η_s [73,74]. In fact, as noted in Ref. [74], incompressible interfaces are rare in practice, and most interfacial phases are generally compressible.

In contrast to Ref. [50], we rewrite Eq. (10) in a format much more compact given by

$$\mathbf{n} \cdot (\boldsymbol{\sigma}_1 - \boldsymbol{\sigma}_2) \cdot \mathbf{n} = -[\gamma + (\kappa_s + \eta_s)\nabla_s \cdot \mathbf{u}]\mathcal{K}, \tag{11}$$

where $\mathcal{K} = \nabla_s \cdot \mathbf{n}$ is the interface curvature in the plane of the Hele-Shaw cell. Note that the curvature in the direction perpendicular to the plates ($\mathcal{K}_\perp = 2/b$) was not considered in Eq. (11) as it is nearly constant [75,76] and hence does not significantly affect the interface motion. As commented earlier, within the scope of the Boussinesq-Scriven model, the fluid-fluid interface is described as a two-dimensional strip. However, since $\mathcal{K}_\perp$ is nearly constant, one can simply keep track of the fluid-fluid deformation just along an effectively one-dimensional interface having in-plane curvature $\mathcal{K}$. Also, it is worth noting that the term $\eta_s(\nabla_s \cdot \mathbf{u})\mathcal{K}$ in Eq. (11) is obtained by rewriting the last line of Eq. (10) as $-2\eta_s(\nabla_s \cdot \mathbf{u})\mathcal{K}$. See Appendix B for details about this calculation. The pressure jump across the interface, $(p_1 - p_2)_{\mathcal{R}}$, arises from Eq. (11) using the stress tensor $\boldsymbol{\sigma}_j$ for a viscous Newtonian, incompressible fluid, which is given by contributions from viscous normal stresses and pressure [77–80]:

$$\boldsymbol{\sigma}_j = -p_j \mathbf{I}_j + \eta_j[\nabla \mathbf{u}_j + (\nabla \mathbf{u}_j)^T]. \tag{12}$$

Substituting the stress tensor (12) into Eq. (11), we have

$$\begin{aligned}(p_1 - p_2)_{\mathcal{R}} = {} & [\gamma + (\kappa_s + \eta_s)\nabla_s \cdot \mathbf{u}]\mathcal{K} \\ & + \mathbf{n} \cdot \{\eta_1[\nabla \mathbf{u}_1 + (\nabla \mathbf{u}_1)^T] \\ & - \eta_2[\nabla \mathbf{u}_2 + (\nabla \mathbf{u}_2)^T]\}_{\mathcal{R}} \cdot \mathbf{n}.\end{aligned} \tag{13}$$

This equation illustrates how surface tension, viscous normal stresses, and interfacial rheology yield a pressure jump across the interface. The first term on the RHS, $\gamma\mathcal{K}$, is commonly known as the Young-Laplace pressure boundary condition [1]. Also, by observing Eq. (13), one verifies that the interfacial rheology contribution [the term with $(\kappa_s + \eta_s)$ on the RHS of Eq. (13)] yields an effective surface tension given by $[\gamma + (\kappa_s + \eta_s)\nabla_s \cdot \mathbf{u}]$. Finally, the last term of Eq. (13) represents the balance of viscous normal stresses at the interface.

Note that we need the fluid velocity at the interface, $\mathbf{u}$, to compute the contribution of the interfacial rheology to the pressure jump in Eq. (13). In this regard, the authors of Ref. [50] take advantage of the fact that they are interested in the linear stability analysis of the interface dynamic. In this regime, as the interface perturbation is much smaller than the interface radius, Ref. [50] assumes that the flow is predominantly radial (i.e., $u_r \gg u_\theta$) in the pressure jump condition [Eq. (13)]. Consequently, in Ref. [50] it is also considered that the interface normal vector $\mathbf{n} \approx \mathbf{e}_r$, where $\mathbf{e}_r$ is the unit vector along the radial direction. Under these circumstances, using the kinematic boundary condition [Eq. (5)], which imposes the continuity of the normal fluid velocities across the interface,

$$\mathbf{n}\cdot\mathbf{u}_1|_{\mathcal{R}}=\mathbf{n}\cdot\mathbf{u}_2|_{\mathcal{R}}, \tag{14}$$

Ref. [50] computes $\mathbf{u}$ assuming it is equal to the radial projection of the velocities of fluids 1 and 2 evaluated at the interface, i.e., $\mathbf{u}\approx u_r\mathbf{e}_r\approx u_{1r}|_{\mathcal{R}}\,\mathbf{e}_r\approx u_{2r}|_{\mathcal{R}}\,\mathbf{e}_r$.

Nevertheless, as the interface perturbations grow, the azimuthal velocity u_θ becomes relevant so one can no longer assume that $\mathbf{u}$ and $\mathbf{n}$ point along $\mathbf{e}_r$. In fact, they should point in an arbitrary direction depending on the interface deformation. This general situation will be considered here since we intend to capture nonlinear effects of the interface dynamics, and thus analyze the formation of viscous fingers slightly larger than those of Ref. [50]. As a first approach to considering an arbitrary $\mathbf{n}$ in the viscous fingering instability under the influence of interfacial rheology, below we calculate $\mathbf{u}$ assuming a flow setup slightly more general than the one considered in Ref. [50].

First, notice that, in reality, the structured rheological interface should be a thin layer, of small but finite thickness (typically of the size of the species constituting it) whose velocity field $\mathbf{v}$ matches $\mathbf{u}_1$ at the inner boundary (*fluid 1-layer*) and $\mathbf{u}_2$ at the outer boundary (*layer-fluid 2*), namely,

$$\mathbf{v}|_{r=\mathcal{R}_1}=\mathbf{u}_1|_{r=\mathcal{R}_1}\ \text{ and }\ \mathbf{v}|_{r=\mathcal{R}_2}=\mathbf{u}_2|_{r=\mathcal{R}_2}, \tag{15}$$

where $\mathcal{R}_1$ and $\mathcal{R}_2$ are the positions of the inner and outer boundaries, respectively. Therefore, given that the layer thickness is much smaller than any length scale of the system (basically a single layer of molecules thick), let us assume that $\mathbf{u}$ can be calculated as the transversal average of $\mathbf{v}$ across the layer.

To calculate the velocity field within the layer, $\mathbf{v}$, let d be the thickness of the thin layer between fluids 1 and 2. Since d is significantly small, first assume that the inner and outer boundaries of the layer are parallel (with normal vector $\mathbf{n}$). Then, define r_n as the distance along $\mathbf{n}$ from the inner boundary to an arbitrary point within the layer. In this manner, $r_n=0$ and $r_n=d$ define the positions of the inner and outer boundaries, respectively. From these definitions and using the fact that d is extremely small, we rewrite the continuity conditions of Eq. (15) as

$$\mathbf{v}(r_n=0)\approx\mathbf{u}_1|_{\mathcal{R}}\ \text{ and }\ \mathbf{v}(r_n=d)\approx\mathbf{u}_2|_{\mathcal{R}}, \tag{16}$$

where it was assumed that $\mathcal{R}_j\approx\mathcal{R}$, with $j=1,2$, on the RHS of Eq. (15). In this framework, by examining Eq. (16) and the continuity of the normal fluid velocities at the effectively one-dimensional interface [see Eq. (14)], we verify that the normal component of $\mathbf{v}$ is approximately constant along $\mathbf{n}$, i.e.,

$$\mathbf{n}\cdot\mathbf{v}(r_n)\approx v_n=u_{1n}|_{\mathcal{R}}=u_{2n}|_{\mathcal{R}}, \tag{17}$$

where $u_{jn}=\mathbf{n}\cdot\mathbf{u}_j$.

To calculate the tangential component of $\mathbf{v}$, first recall that in the description of an effectively one-dimensional interface, the tangential projection of $\mathbf{u}_j$ is discontinuous as one crosses the interface, in contrast to the normal component of $\mathbf{u}_j$. This discontinuity is extensively explored in the vortex-sheet formalism [3], where the vorticity on the interface is quantified by the vortex-sheet "strength" $\mathbf{s}\cdot(\mathbf{u}_1-\mathbf{u}_2)_{\mathcal{R}}$, with $\mathbf{s}$ being the unit tangent vector to $r=\mathcal{R}(\theta,t)$. Note that $\mathbf{s}$ should also be tangent to the inner and outer boundaries since they are parallel and very close to each other. In this scenario, from the continuity conditions (16), we see that, differently from v_n, $v_s=\mathbf{s}\cdot\mathbf{v}$ cannot be a constant vector. Thus, as d is significantly small, let us consider that v_s is approximately a linear function of r_n, with boundary conditions given by Eq. (16), i.e.,

$$v_s(r_n)\approx\frac{(u_{2s}-u_{1s})_{\mathcal{R}}}{d}r_n+u_{1s}|_{\mathcal{R}}, \tag{18}$$

where $u_{js}=\mathbf{s}\cdot\mathbf{u}_j$. Notice that $v_s(0)=u_{1s}|_{\mathcal{R}}$ and $v_s(d)=u_{2s}|_{\mathcal{R}}$.

Finally, considering that $\mathbf{u}$ is the transversal average of $\mathbf{v}(r_n)=v_n\mathbf{n}+v_s(r_n)\mathbf{s}$ across the interface layer, we have

$$\mathbf{u}\approx\frac{1}{d}\int_0^d\mathbf{v}(r_n)dr_n=\frac{(\mathbf{u}_1+\mathbf{u}_2)_{\mathcal{R}}}{2}. \tag{19}$$

Equation (19) tells us that, within the approach of an effectively one-dimensional interface, the fluid velocity at this boundary is approximately the average of the velocities of fluids 1 and 2. From now on, we will focus exclusively on the effective one-dimensional interface $r=\mathcal{R}(\theta,t)$, using Eq. (19) as the fluid velocity at this boundary. With this expression for $\mathbf{u}$ in hand, we can finally conclude our calculation of the pressure jump in Eq. (13).

Substituting Eq. (19) into (13), at last we obtain $(p_1-p_2)_{\mathcal{R}}$ in the desired format to compute the interface dynamic equation via Eq. (4):

$$\begin{aligned}(p_1-p_2)|_{\mathcal{R}}=&\left[\gamma+\frac{\kappa_s+\eta_s}{2}[\boldsymbol{\nabla}_s\cdot(\mathbf{u_1}+\mathbf{u_2})]_{\mathcal{R}}\right]\mathcal{K}\\&+\mathbf{n}\cdot\{\eta_1[\boldsymbol{\nabla}\mathbf{u}_1+(\boldsymbol{\nabla}\mathbf{u}_1)^T]-\eta_2[\boldsymbol{\nabla}\mathbf{u}_2+(\boldsymbol{\nabla}\mathbf{u}_2)^T]\}_{\mathcal{R}}\cdot\mathbf{n}.\end{aligned} \tag{20}$$

The contribution of interfacial rheology showed in Eq. (20) can be rewritten in terms of the velocity potentials by using $\mathbf{u}_j=-\boldsymbol{\nabla}\phi_j$,

$$\begin{aligned}[\boldsymbol{\nabla}_s\cdot(\mathbf{u_1}+\mathbf{u_2})]_{\mathcal{R}}=&-\frac{n_r^2}{r}\left(\frac{\partial\phi_1}{\partial r}+\frac{1}{r}\frac{\partial^2\phi_1}{\partial\theta^2}\right)-n_\theta^2\frac{\partial^2\phi_1}{\partial r^2}\\&-2n_rn_\theta\left(\frac{1}{r^2}\frac{\partial\phi_1}{\partial\theta}-\frac{1}{r}\frac{\partial^2\phi_1}{\partial r\partial\theta}\right)\\&-\frac{n_r^2}{r}\left(\frac{\partial\phi_2}{\partial r}+\frac{1}{r}\frac{\partial^2\phi_2}{\partial\theta^2}\right)-n_\theta^2\frac{\partial^2\phi_2}{\partial r^2}\\&-2n_rn_\theta\left(\frac{1}{r^2}\frac{\partial\phi_2}{\partial\theta}-\frac{1}{r}\frac{\partial^2\phi_2}{\partial r\partial\theta}\right),\end{aligned} \tag{21}$$

where n_r and n_θ denote the radial and azimuthal components of the unit normal vector to the interface. The influence of viscous normal stresses on $(p_1-p_2)_{\mathcal{R}}$ can also be expressed in terms of ϕ_j as

$$\begin{aligned}&\mathbf{n}\cdot\{\eta_1[\boldsymbol{\nabla}\mathbf{u}_1+(\boldsymbol{\nabla}\mathbf{u}_1)^T]-\eta_2[\boldsymbol{\nabla}\mathbf{u_2}+(\boldsymbol{\nabla}\mathbf{u}_2)^T]\}_{\mathcal{R}}\cdot\mathbf{n}\\&\quad=2\eta_2\left[n_r^2\frac{\partial^2\phi_2}{\partial r^2}+2\frac{n_rn_\theta}{r}\left(\frac{\partial^2\phi_2}{\partial r\partial\theta}-\frac{1}{r}\frac{\partial\phi_2}{\partial\theta}\right)\right.\end{aligned}$$

$$+\frac{n_\theta^2}{r}\left(\frac{\partial\phi_2}{\partial r}+\frac{1}{r}\frac{\partial^2\phi_2}{\partial\theta^2}\right)\bigg]$$

$$-2\eta_1\left[n_r^2\frac{\partial^2\phi_1}{\partial r^2}+2\frac{n_r n_\theta}{r}\left(\frac{\partial^2\phi_1}{\partial r\partial\theta}-\frac{1}{r}\frac{\partial\phi_1}{\partial\theta}\right)\right.$$

$$\left.+\frac{n_\theta^2}{r}\left(\frac{\partial\phi_1}{\partial r}+\frac{1}{r}\frac{\partial^2\phi_1}{\partial\theta^2}\right)\right]. \tag{22}$$

A detailed derivation of Eq. (22) is given in Appendix A of Ref. [81] (see also Appendix B in Ref. [50]). An equivalent expression was originally obtained in Ref. [82] [see Eq. (4) of this reference], but their expression misses the factors of 2 that multiply the terms $n_r n_\theta$ on the RHS of Eq. (22). In addition, it is worth pointing out that Refs. [81,82] investigated the influence of viscous normal stresses on viscous fingering instability without considering interfacial rheology.

Equation (20), jointly with Eqs. (21) and (22), offers a generalization for Eq. (10) of Ref. [50], with the unit normal vector having an arbitrary direction and the fluid velocity at the interface being the average of $\mathbf{u}_1|_{\mathcal{R}}$ and $\mathbf{u}_2|_{\mathcal{R}}$. We now have all the central physical ingredients to properly investigate the weakly nonlinear dynamics of the interface $r=\mathcal{R}(\theta,t)$. This will be done in Sec. II B.

B. The mode-coupling dynamic equation

The goal of this section is to derive a second-order mode-coupling equation for the deformed fluid-fluid interface $r=\mathcal{R}(\theta,t)$. We begin representing $\mathcal{R}(\theta,t)$ as

$$\mathcal{R}(\theta,t)=R(t)+\zeta(\theta,t), \tag{23}$$

where $\zeta=\zeta(\theta,t)$ is the interface perturbation and

$$R(t)=\sqrt{R_0^2+\frac{Qt}{\pi}} \tag{24}$$

is the time-dependent unperturbed radius of the two-fluid interface, with R_0 being the unperturbed interface radius at $t=0$. To capture the early nonlinear stages of the dynamics of $\mathcal{R}=\mathcal{R}(\theta,t)$, we will consider terms up to second order in ζ. Expanding the perturbation of the fluid-fluid interface in Fourier series, we have

$$\zeta(\theta,t)=\sum_{n=-\infty}^{+\infty}\zeta_n(t)\exp{(in\theta)}, \tag{25}$$

where $\zeta_n(t)$ are the complex Fourier amplitudes with integer wave numbers n. In this framing, the weakly nonlinear evolution of the interface is described by a mode-coupling differential equation for the perturbation amplitudes $\zeta_n(t)$. Note that in Eq. (25) the $n=0$ mode is included to maintain the area of the perturbed shape independent of the perturbation ζ. Then, mass conservation imposes that the zeroth mode is written in terms of the other modes as $\zeta_0=-(1/2R)\sum_{n\neq0}|\zeta_n(t)|^2$ [9]. Note that the area constraint expressed by ζ_0 couples the mode $n=0$ with all other modes $n\neq0$ and depends on the Fourier amplitudes squared, indicating that it is an intrinsically a nonlinear concern, not required in linear stability analysis.

With the interface description given by Eqs. (23)–(25), we turn our attention back to the dynamic equation of the interface (4). The velocity potentials appearing on the left-hand side of Eq. (4) are calculated from Eq. (3), whose solutions are

$$\phi_j=-\frac{Q}{2\pi}\ln\left(\frac{r}{R}\right)+\sum_{n\neq0}\phi_{jn}(t)\left(\frac{r}{R}\right)^{(-1)^{(j+1)}|n|}\exp{(in\theta)}. \tag{26}$$

The velocity potentials become completely determined by expressing the Fourier amplitudes $\phi_{jn}(t)$ of Eq. (26) in terms of the interface perturbation amplitudes $\zeta_n(t)$ given in Eq. (25). To this end, we use the kinematic boundary condition (5), expanding it up to second order in ζ. Then, Fourier transforming the resulting expression and solving it for $\phi_{jn}(t)$ consistently to second order, we obtain expressions for $\phi_{jn}(t)$ related to $\zeta_n(t)$, and its time derivative $\dot{\zeta}_n(t)$ where the overdot represents a total time derivative. With the solutions for $\phi_{jn}(t)$ placed into Eq. (26), we substitute ϕ_j into the interface dynamic Eq. (4) and the pressure jump (20), always keeping terms up to second order in ζ.

Now we need to plug the pressure boundary condition (20) into Eq. (4), expressing $\mathcal{K}=\boldsymbol{\nabla}_s\cdot\mathbf{n}$ in terms of ζ. As mentioned earlier, $\mathcal{K}$ designates the interface curvature in the plane of the cell [1], and it is related to $\mathcal{R}$ via

$$\mathcal{K}=\frac{\mathcal{R}^2+2\left(\frac{\partial\mathcal{R}}{\partial\theta}\right)^2-\mathcal{R}\frac{\partial^2\mathcal{R}}{\partial\theta^2}}{\left[\mathcal{R}^2+\left(\frac{\partial\mathcal{R}}{\partial\theta}\right)^2\right]^{3/2}}. \tag{27}$$

Finally, after substituting the solution (26) and Eq. (20) into the equation of motion (4), we keep terms up to second-order in ζ and Fourier transform. As a result, we obtain a dimensionless mode-coupling differential equation for the perturbation amplitudes (for $n\neq0$) given by

$$\dot{\zeta}_n=\lambda(n)\zeta_n+\sum_{n'\neq0}\{[F(n,n')+F_S(n,n')+F_R(n,n')]\zeta_{n'}\zeta_{n-n'}$$

$$+[G(n,n')+G_S(n,n')+G_R(n,n')]\dot{\zeta}_{n'}\zeta_{n-n'}\}, \tag{28}$$

where

$$\lambda(n)=\frac{1}{s(n)}\left\{\frac{1}{2\pi R^2}(A|n|-1)-\frac{(A+1)}{2\text{Ca}R^3}|n|(n^2-1)\right.$$

$$\left.-\frac{1}{12\pi R^4}|n|(|n|-A)-\frac{\text{Bq}(A+1)}{48\pi R^5}|n|(n^2-2)\right\} \tag{29}$$

is the linear growth rate. Besides,

$$s(n)=1+\frac{1}{6R^2}|n|(|n|+A)+\frac{\text{Bq}(A+1)}{24R^3}|n|, \tag{30}$$

$$\text{Ca}=\frac{12\eta_2 Q}{\gamma b} \tag{31}$$

is the global capillary number [81] which expresses a relative measure of viscous to surface tension forces, and

$$\mathrm{Bq} = \frac{\kappa_s}{\eta_2 b} \tag{32}$$

is a Boussinesq number which measures the relative strength of surface viscous stresses to bulk (outer fluid) viscous stress. As in Ref. [50], here we consider that the dilational viscosity is much bigger than the surface shear viscosity, $\kappa_s \gg \eta_s$ [83–85]. Notice that by taking the limit $\mathrm{Bq} \to 0$ in Eq. (28), the surface rheology effects vanish, and one recovers the results of Refs. [81,82]. In addition, observe that Ref. [50] defines the Boussinesq number of Eq. (32) by using the symbol Bq_b. In this manner, Bq in Ref. [50] is a modified Boussinesq number that is about 10–1000 times larger than our Bq as defined in Eq. (32).

The second-order terms of Eq. (28) characterize the early nonlinear stages of the interface dynamic. Among these functions, F_R and G_R represent the contributions from interfacial rheology, and F_S and G_S originate from viscous normal stresses. The expressions for all the nonlinear mode-coupling functions F, F_S, F_R, G, G_S, and G_R are given in Appendix C—see Eqs. (C1)–(C6). In Eq. (28), lengths are rescaled by b and velocities by Q/b. We emphasize that all dimensionless parameters we use throughout this paper are consistent with typical physical quantities used in real experiments of injection-driven, radial Hele-Shaw flows [1,7,8,10,11,30].

Finally, to have a consistent second-order mode-coupling equation, we replace the time derivative terms $\dot{\zeta}_{n'}$ appearing on the RHS of Eq. (28) by $\lambda(n')\zeta_{n'} + O(\zeta_{n'}^2)$ to finally obtain

$$\begin{aligned}\dot{\zeta}_n = \lambda(n)\zeta_n + \sum_{n'\neq 0}\{[F(n,n') + F_S(n,n') + F_R(n,n')]\\ + \lambda(n')[G(n,n') + G_S(n,n') + G_R(n,n')]\}\zeta_{n'}\zeta_{n-n'}.\end{aligned} \tag{33}$$

This is the second-order mode-coupling equation for the fluid-fluid interface in a radial injection-driven flow, taking into account the action of interfacial rheology. We point out that, over the years, fully nonlinear numerical studies for various other pattern formation systems [67,68,86–90] have validated the weakly nonlinear method used in this section. These fully nonlinear studies reveal that the weakly nonlinear theory can accurately describe the beginning of pattern formation, providing a reliable approach to predict fundamentally important, fully nonlinear, pattern-forming mechanisms.

III. DISCUSSION

In this section, we utilize our perturbative, second-order mode-coupling theory to examine how the finger tip-splitting phenomena are influenced by interfacial rheology effects at early nonlinear stages of radial Hele-Shaw flows. To do it, we use the nonlinear, coupled differential equations for the perturbation amplitudes [Eq. (33)] and rewrite the complex interfacial perturbation given in Eq. (25) in terms of cosine and sine modes

$$\zeta(\theta,t) = \zeta_0 + \sum_{n=1}^{\infty}[a_n(t)\cos n\theta + b_n(t)\sin n\theta], \tag{34}$$

where $a_n(t) = \zeta_n(t) + \zeta_{-n}(t)$ and $b_n(t) = i[\zeta_n(t) - \zeta_{-n}(t)]$ are real valued. In addition, we have that

$$\zeta_0 = -\frac{1}{4R}\sum_{n=1}^{\infty}\left[a_n^2(t) + b_n^2(t)\right]. \tag{35}$$

To generate the shape of the time-evolving interfacial patterns, we consider the nonlinear coupling of a finite number of Fourier modes, and from Eq. (33) obtain the corresponding versions of the mode-coupling differential equations for the mode amplitudes $a_n(t)$ and $b_n(t)$. The time evolution for $a_n(t)$ and $b_n(t)$ gives the time evolution for the interface itself [from Eqs. (23) and (34)]. The resulting set of coupled nonlinear differential equations for these real-valued amplitudes is numerically solved by using the software package MATHEMATICA 12.1.

It is well established from previous weakly nonlinear studies of the Saffman-Taylor problem [6,9] that the tip-splitting mechanism in Hele-Shaw flows can be properly emulated by considering the weakly nonlinear coupling of just two particularly relevant Fourier modes: a fundamental mode n and its first-harmonic $2n$. Thus, in the context of such a simplified perturbative mode-coupling picture, the tip-splitting phenomena are produced by the nonlinear influence of the fundamental mode n on the growth of the harmonic mode $2n$. Within this approach, the fundamental mode sets the overall n-fold symmetric morphology of the pattern, while the first harmonic mode $2n$ determines the specific shape of the finger tips (namely, if the tips are narrow, wide, or if they split). In Fig. 2, we use this simple mode-coupling scheme involving only modes n and $2n$ to gain insight into how surface rheological stresses act on the development of finger tip splitting at early nonlinear dynamical stages of radial fingering.

Figure 2 illustrates the fluid-fluid interface time evolution for $0 \leqslant t \leqslant t_f$, considering the interaction of the Fourier modes n and $2n$, where the various interfaces of each pattern are plotted in equal time intervals $\Delta t = t_f/10$, with t_f denoting the largest time before successive interfaces cross one another [91]. This interface crossing is not observed in high viscosity contrast radial Hele-Shaw cell experiments [1,7,8,10,11,30]. Therefore, the largest time before crossing is used as the upper bound time ($t = t_f$) for the applicability of our perturbative description. The interfacial patterns portrayed in Fig. 2 are produced by considering the following characteristic dimensionless parameter values: $A = 1$, $\mathrm{Ca} = 150$, $R_0 = 3$, and $\mathrm{Bq} = 0, 15, 30$. The choice for this specific viscosity contrast value ($A = 1$, where $0 < A \leqslant 1$) is mainly motivated by its wide use in radial viscous fingering experiments [1,7,8,10,11,30], but also because such a large viscosity contrast induces significant interface destabilization, favoring the occurrence of tip-splitting events. Moreover, if Ca is too small, the interface is quite stable against perturbations, making its time evolution uninteresting. However, if Ca is very large the interface becomes very quickly deformed, creating difficulties for an accurate early nonlinear theoretical description, since the undesired (and, unphysical) interface crossings occur rapidly. For these reasons, we have chosen a relatively small value for the capillary number $\mathrm{Ca} = 150$ (where typically $O(10) \leqslant \mathrm{Ca} \leqslant O(10^3)$ [1,7,8,10,11,30]). This is done to prevent a sudden, excessive growth of the interface,

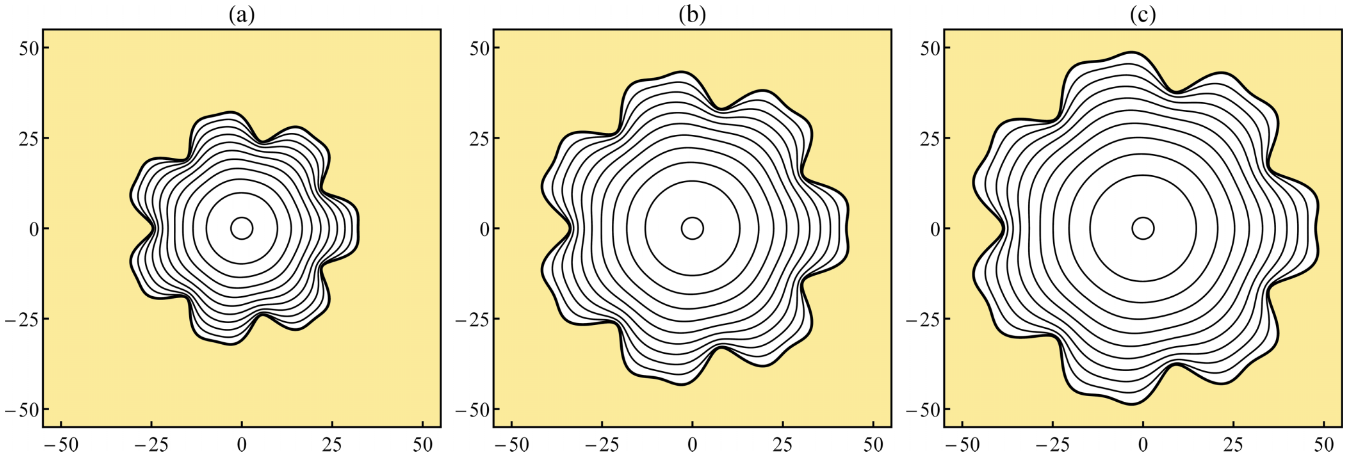

FIG. 2. Time evolution of the weakly nonlinear interfacial patterns generated by solving Eq. (33) for $0 \leqslant t \leqslant t_f$, and three increasingly larger values of the Boussinesq number (a) Bq = 0, (b) Bq = 15, and (c) Bq = 30. For a given Bq, the final time t_f is the maximum allowed time before unphysical interface crossings begin. These final times are (a) $t_f = 2754$, (b) $t_f = 5087$, and (c) $t_f = 6499$. Interface profiles are plotted in time intervals of $t_f/10$, where the interface at $t = t_f$ is depicted by a thicker curve in black. The viscous outer fluid is represented by the shaded region, and the inner fluid of negligible viscosity is represented by the white region. Here we consider the second-order nonlinear coupling of cosine modes, where the fundamental mode $n = n_{\max}^{\zeta} = 7$, with its harmonic $2n = 14$. The other flow parameters are $A = 1$, Ca = 150, and $R_0 = 3$. The initial perturbation amplitudes are $a_n(0) = R_0/2500$ and $a_{2n}(0) = 0$

leading us very quickly to a regime in which our perturbative approach would not be valid (perturbatively, we must have $|\zeta_n(t)|/R(t) \ll 1$). We also note there is nothing particularly special about the value we have taken for R_0 [$R_0 = 3$, where $O(1) \leqslant R_0 \leqslant O(10)$], other than it lies within of the range of typical values used in the radial flow experiments mentioned above. Finally, we point out that the values for the Boussinesq number we use (Bq = 0, 15, 30) are fully consistent with the corresponding magnitudes of Bq utilized in Ref. [50]. In this framing, the final times are $t_f = 2754$ [Fig. 2(a)], $t_f = 5087$ [Fig. 2(b)], and $t_f = 6499$ [Fig. 2(c)].

To generate the patterns illustrated in Fig. 2, we follow Ref. [92] and choose the fundamental mode to be the mode of largest interfacial amplitude when Bq = 0, as given by linear stability analysis, i.e., $n = n_{\max}^{\zeta}$ taken at time t_f, and obtained by maximizing the linear perturbation amplitude $\zeta_n(t)$. For the parameters considered in Fig. 2, we find that $n = n_{\max}^{\zeta} = 7$, therefore $2n = 14$. It has been shown in Ref. [9] that when only the modes n and $2n$ are considered at second order, there is no coupling between the sine mode amplitude b_{2n} and the cosine mode amplitude a_n, so the growth of b_{2n} is uninfluenced by a_n. In this way, for the purposes of our simplified mode-coupling picture shown in Fig. 2, the finger tip-splitting phenomenon can be described and captured by considering the coupling of the cosine mode amplitudes. Therefore, without loss of generality, in the pattern-forming structures displayed in Fig. 2, just cosine modes are considered and $b_n(t) = b_{2n}(t) = 0$. Moreover, to ensure that the morphological features of the patterns depicted in Fig. 2 are spontaneously induced by the weakly nonlinear dynamics and not imposed by a large initial amplitude for the cosine harmonic mode $2n$, we set the initial ($t = 0$) harmonic mode amplitude to zero [$a_{2n}(0) = 0$]. In this way, at $t = 0$ only the fundamental mode n has a nonzero, but small amplitude given by $a_n(0) = R_0/2500$. Under these circumstances, and utilizing Eq. (33), the equations of motion for the cosine amplitudes for modes $2n$ and n are

$$\dot{a}_{2n} = \lambda(2n)a_{2n} + \tfrac{1}{2}\Lambda(2n, n)a_n^2 \tag{36}$$

and

$$\dot{a}_n = \lambda(n)a_n + \tfrac{1}{2}\Lambda(n, 2n)a_n a_{2n}, \tag{37}$$

where

$$\Lambda(n, p) = F(n, p) + F_S(n, p) + F_R(n, p) + \lambda(p)[G(n, p) + G_S(n, p) + G_R(n, p)]. \tag{38}$$

The time evolution of the amplitudes $a_n(t)$ and $a_{2n}(t)$ is obtained by numerically solving the coupled nonlinear differential equations (36) and (37). Within the scope of second-order mode coupling, it is known that an enhanced tendency of the fingers to get wider (narrower) occurs when $a_{2n} < 0$ ($a_{2n} > 0$) [9]. Therefore, a negative growth for the cosine amplitude of the first harmonic mode $2n$ would mean a tendency toward finger tip-splitting formation.

In Fig. 2, we illustrate the weakly nonlinear pattern morphologies that arise if surface rheological effects are neglected [Fig. 2(a)] or taken into consideration [Fig. 2(b) and Fig. 2(c)] under the simplified scenario in which only cosine modes n and $2n$ are present. As one can see by examining Fig. 2(a) for the situation in which interfacial rheology is neglected (Bq = 0), we have the formation of a sevenfold pattern whose overall shape is determined by the fundamental mode $n = 7$. As time advances, one observes that the growing fingers widen, ultimately leading to the emergence of fingered structures having flat tips that are about to split. These finger tip-widening and -flattening processes are provoked by the enhanced nonlinear growth of the first-harmonic mode $2n$, preluding the occurrence of finger tip splitting. These findings are in line with the theoretical predictions of Ref. [9], as well as with the experimental results of Refs. [1,7,8,10,11,30].

We proceed by inspecting Fig. 2(b), which displays the interface evolution when interfacial rheology is taken into account and $\mathrm{Bq} = 15$. The most evident feature of the pattern depicted in Fig. 2(b) is that although we still have the formation of a seven-fingered structure, contrary to what happened in Fig. 2(a), now the fingers get wider and wider and eventually bifurcate at their tips, clearly exhibiting the occurrence of finger tip splitting. These finger tip-splitting events have been induced by the action of surface rheological stresses.

It should be pointed out that in Fig. 2(a) $t_f = 2754$ and that in Fig. 2(b) $t_f = 5087$. Thus, in Fig. 2(b), when surface rheological stresses are present, one can evolve the interface dynamics up to larger times, still avoiding the undesirable crossing between successive interfaces. This is the reason why the pattern obtained in Fig. 2(b) for $\mathrm{Bq} = 15$ has a larger size than the one shown in Fig. 2(a) for $\mathrm{Bq} = 0$. This overall stabilizing effect introduced by interfacial rheology stresses is entirely consistent with the linear stability results of Ref. [50], where it has been found that surface rheological stresses tend to stabilize radial fingering at linear stages of the flow. Nevertheless, if on one hand it is true that interfacial rheology slows down the growth of the pattern as a whole, on the other hand the delayed fingers become more bifurcated than those generated when $\mathrm{Bq} = 0$. Therefore, the analysis of Figs. 2(a) and 2(b) indicate that regardless of the stabilizing role detected by linear theory, at the nonlinear level such surface rheological stresses enhance the tip-splitting instability.

These conclusions are reinforced by the examination of Fig. 2(c), which presents the pattern evolution for a larger Boussinesq number ($\mathrm{Bq} = 30$), for which $t_f = 6499$. Indeed, the most salient aspect of the pattern portrayed in Fig. 2(c) is the rising of even stronger finger tip-splitting events than those detected in Fig. 2(b). So, larger values of Bq result in a larger pattern for which the resulting fingers are wider and reveal an enhanced tendency toward finger tip-doubling behavior.

Figure 3 compares the time evolution of the rescaled cosine amplitudes for the fundamental (first harmonic) mode $a_n(t)/R(t)$ [$a_{2n}(t)/R(t)$] related to the weakly nonlinear patterns shown in Fig. 2, for three increasing values of the Boussinesq number $\mathrm{Bq} = 0, 15, 30$. First, we observe that regardless of the value of Bq, the weakly nonlinear coupling between modes n and $2n$ dictates the sign of the harmonic mode, going negative despite its initial amplitude value being zero [$a_{2n}(0) = 0$]. This is precisely the sign of the harmonic mode that leads to finger-tip broadening, finger-tip flattening, and then to finger tip splitting [9]. In addition, notice that the attenuated growth of the fundamental for larger values of Bq allows one to evolve the patterns' growth up to larger times avoiding interfaces crossings, as commented on earlier in our discussion of Fig. 2. However, by examining Fig. 3, it is difficult to conclude that when $\mathrm{Bq} > 0$, the delayed fingers arise more bifurcated than those for $\mathrm{Bq} = 0$, as seen in the patterns of Fig. 2. Instead, we see in Fig. 3 a translation of the curves to longer times when higher values of Bq are considered, with the ratio between the amplitudes of the first harmonic a_{2n} and the fundamental mode a_n not changing significantly.

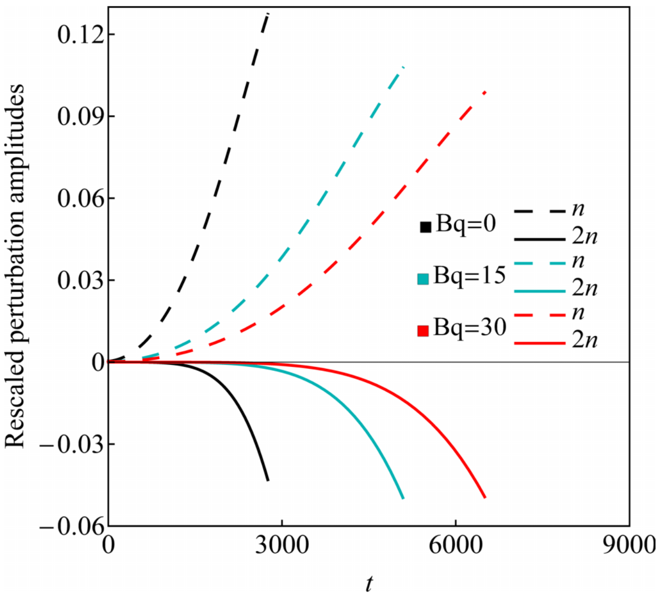

FIG. 3. Time evolution of the rescaled cosine interfacial amplitudes for the fundamental mode $a_n(t)/R(t)$ (dashed curves) and for the first-harmonic mode $a_{2n}(t)/R(t)$ (solid curves) associated with the weakly nonlinear patterns illustrated Fig. 2, for increasing values of the Boussinesq number: $\mathrm{Bq} = 0, 15, 30$.

The enhancement of finger tip splitting when surface rheological effects are more intense can be quantitatively verified in Fig. 4. Here, this is illustrated with a parametric plot expressing the behavior of $a_{2n}(t)/R(t)$ relative to $a_n(t)/R(t)$ as time advances in the interval $0 \leqslant t \leqslant t_f$ for the pattern growth situations depicted in Fig. 2. This particular type of plot (for which time t is the parameter) is useful to compare pattern morphologies for situations involving different values of the Bq, since $a_n(t)/R(t)$ is associated with the average size and overall n-fold symmetry of the

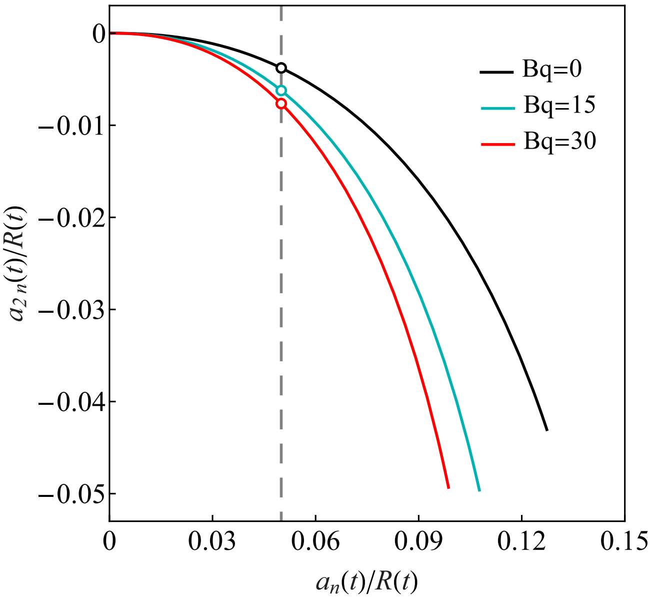

FIG. 4. Behavior of $a_{2n}(t)/R(t)$ with respect to $a_n(t)/R(t)$ for the pattern evolutions depicted in Fig. 2, for different values of the Boussinesq number: $\mathrm{Bq} = 0, 15, 30$. The vertical dashed line is drawn for $a_n(t)/R(t) = 0.05$.

patterned structures, while $a_{2n}(t)/R(t)$ is linked to the specific shape of the finger tip (i.e., if the tips are wide and split or if they are narrow and get sharper). By examining Fig. 4, it is evident that as $a_n(t)/R(t)$ is increased, $a_{2n}(t)/R(t)$ tends to become more and more negative, favoring finger tip widening and tip splitting. By inspecting Fig. 4, one can also see that, for any given value of $a_n(t)/R(t)$, the corresponding value of $a_{2n}(t)/R(t)$ is more negative for larger Bq. This can be easily identified in Fig. 4, for instance, by following the intersection points (open circles) of the vertical dashed line for $a_n(t)/R(t) = 0.05$ with the curves for different Bq. These remarks support our conclusions extracted from Fig. 2, indicating that interfacial rheology effects delay the occurrence of tip-splitting events, but when these events do take place, they are more intense for larger values of the Boussinesq number Bq.

Irrespective of the relevance of the weakly nonlinear predictions extracted from the analysis of Figs. 2–4, the scenario contemplated in these plots is somewhat idealized, in the way that just two particular modes are present (fundamental n and its first-harmonic $2n$) and specific initial conditions are considered, resulting in the emergence of fairly symmetric n-fold patterns for which finger tip splitting ultimately arises as a prevalent morphological feature.

From this point onward, our major goal is to try to verify the robustness of the weakly nonlinear results captured from Figs. 2–4 by exploring more realistic pattern-forming circumstances. To do that, we follow a successful model originally proposed by Cardoso and Woods [93] for evolving interfaces in the linear stage (their model B), and extended by Miranda and Widom [9] to the weakly nonlinear regime. This model is in consonance with typical conditions of real experiments in radial Hele-Shaw flows [1,7,8,10,11,30] and explores the effect of a background level of noise (for instance, coming from irregularities in the gap thickness b, inhomogeneities on surfaces of the Hele-Shaw cell plates or even from thermal or pressure fluctuations [91]) on the dynamics of the growing interface. Taking these issues into account, the model describes the behavior of the interface separating the fluids, assuming the presence of a constant low level of noise during its entire evolution. In this framework, each participating Fourier mode n is perturbed with a constant (in time) random complex amplitude $\zeta_n(0)$ which contains an n dependent random phase, whose magnitude $|\zeta_n(0)|$ is independent of n by assumption. As the interface expands radially, it successively reaches critical radii $R_c(n)$ [obtained by setting $\lambda(n) = 0$] for each mode n, such that only once a particular $R_c(n)$ is reached, the perturbation amplitude ζ_n starts to vary with time. The predictions of this model are in good agreement with experimental observations within the linear [93] and weakly nonlinear [9] regimes.

Moreover, in all the interfacial patterns presented in the remainder of this paper, we will not be restricted to include only two Fourier modes, but more reasonably and more generally consider the participation of all Fourier modes which lie within the band of unstable modes at time $t = t_f$. Unless a statement to the contrary is made, as we also did in Fig. 2, in the rest of this paper we continue to consider a representative set of dimensionless parameters Ca = 150, $A = 1$, $R_0 = 3$, which are in line with physical values commonly used in many radial Hele-Shaw cell experiments [1,7,8,10,11,30]. Furthermore, in Figs. 5 and 6, we take the noise amplitude $|\zeta_n(0)| = R_0/750$.

Under these circumstances, we consider a whole range of participating Fourier modes $1 \leqslant n \leqslant 25$. Recall that the mode $n = 0$ is written in terms of the other modes via Eq. (35). Although we illustrate our main results by focusing on a representative set of parameters, the reproducibility of the results is tested, generating them by using different initial conditions, in particular, by changing the random phases attributed to each mode [9,91,93]. By doing this, we can directly verify the robustness of our weakly nonlinear results if such conditions are changed.

Keeping in mind the important information given in the previous paragraphs, in Fig. 5 we plot the second-order interface evolutions, when interfacial rheology effects are neglected [(a), (d), (g) for Bq = 0], and taken into account [(b), (e), (h) for Bq = 15], and [(c), (f), (i) for Bq = 30]. To lend support to our theoretical results, three distinct sets of random phases are examined, a first (set I) for (a)–(c), a second (set II) for (d)–(f), and a third (set III) for (g)–(i). It should be noted that the representative patterns depicted in Fig. 5 have been selected from a number of different sets of random phases. We emphasize that, for all multiple sets of phases tested, the general morphological features of the resulting fingers are similar to those exhibited by the representative examples shown in Fig. 5. The values of the final times t_f for the patterns generated in Fig. 5 are (a) 1076, (b) 1867, (c) 2423, (d) 983, (e) 1726, (f) 2210, (g) 1144, (h) 1958, and (i) 2461. Note that for each phase considered, the values of t_f increase as Bq is augmented. As already commented on earlier, this is a consequence of the linearly stabilizing effect induced by interfacial rheology effects [50], which have the tendency to slow down interfacial pattern growth.

By scrutinizing the various structures displayed in Fig. 5, we observe the formation of typical viscous fingering patterns in which seven or eight main fingers of various sizes grow. Interestingly, one can verify that for all three sets of phases considered, some of the fingers tend to get increasingly wider, and flatter at their tips as time advances. In particular, one can notice that some of the flattened tip fingers begin to split via a tip-doubling mechanism. This can been seen by focusing on the fingers indicated by small arrows in Figs. 5(c), 5(f), and 5(i).

It is also clear that finger tip-widening and tip-splitting phenomena are increasingly favored for larger values of the Boussinesq number Bq. As predicted by the simplified situation discussed in Fig. 2, in Fig. 5 we also identify the formation of finger tip-widening and tip-splitting events induced by the action of interfacial rheology effects. Nevertheless, differently from what happened in Fig. 2, where only two predetermined Fourier modes interact in the absence of noise, in Fig. 5 tip-widening and -splitting events continue to be observed, but now under much more realistic circumstances in which one has the presence and nonlinear interaction of a full range of unstable competing modes, as well as the action of random noise. Our second-order mode-coupling results illustrated in Fig. 5 reveal that interfacial rheology stresses play a twofold role regarding interface growth in radial Hele-Shaw flows: If at linear order these stresses act to restrain the overall growth

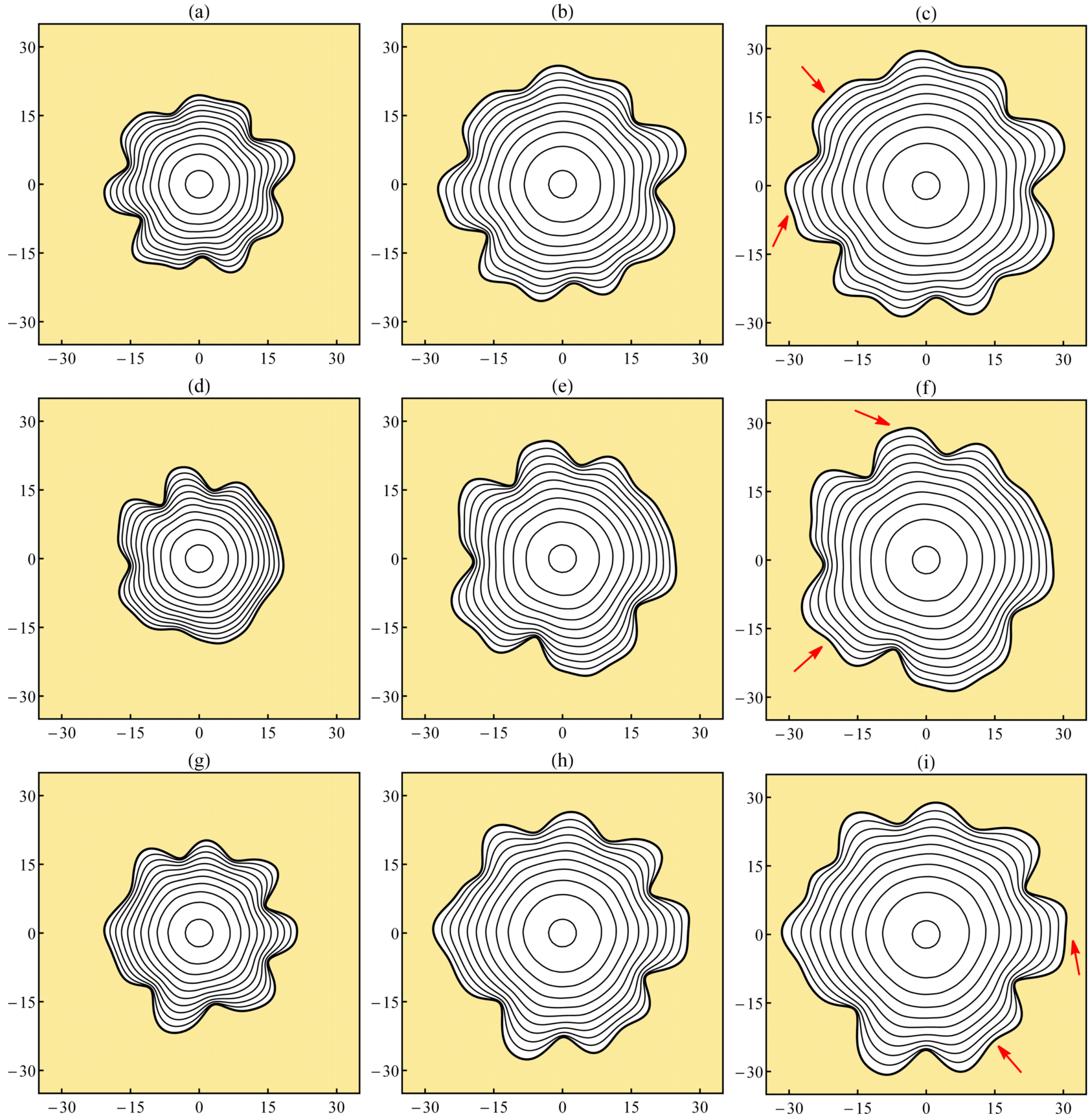

FIG. 5. Time evolution of the weakly nonlinear interfacial patterns generated by solving Eq. (33) for $1 \leqslant n \leqslant 25$, $0 \leqslant t \leqslant t_f$, and equal time intervals $\Delta t = t_f/10$. The patterns are obtained for $\mathrm{Bq} = 0$ [(a), (d), (g)], $\mathrm{Bq} = 15$ [(b), (e), (h)], and $\mathrm{Bq} = 30$ [(c), (f), (i)]. In addition, the values of t_f are (a) 1076, (b) 1867, (c) 2423, (d) 983, (e) 1726, (f) 2210, (g) 1144, (h) 1958, and (i) 2461. Three different sets of random phases are used, set I for [(a)–(c)], set II for [(d)–(f)], and set III for [(g)–(i)]. The most prominent occurrences of finger tip-widening and finger tip-splitting events in (c), (f), and (i) for the largest value of the Boussinesq number considered ($\mathrm{Bq} = 30$) are indicated by small arrows. Here $A = 1$, $\mathrm{Ca} = 150$, and $R_0 = 3$.

of the patterns, at the weakly nonlinear level they operate to favor the occurrence of finger tip widening and tip splitting.

We conclude our discussion by demonstrating the importance of developing a weakly nonlinear analysis of the system to be able to predict and extract useful information on the impact of interfacial rheology effects on the morphology of the viscous fingering structures, in particular, on the occurrence of finger tip widening, flattening, and splitting. Figure 6 compares the linear [(a)–(c)] and weakly nonlinear [(d)–(f)] time evolutions of the viscous fingering patterns for the case of largest Boussinesq number ($\mathrm{Bq} = 30$) utilized in Fig. 5. In Fig. 6, all physical parameters and random phases are identical to those used in Fig. 5. More specifically, in Fig. 6 set I of the random phases is used in (a) and (d), set

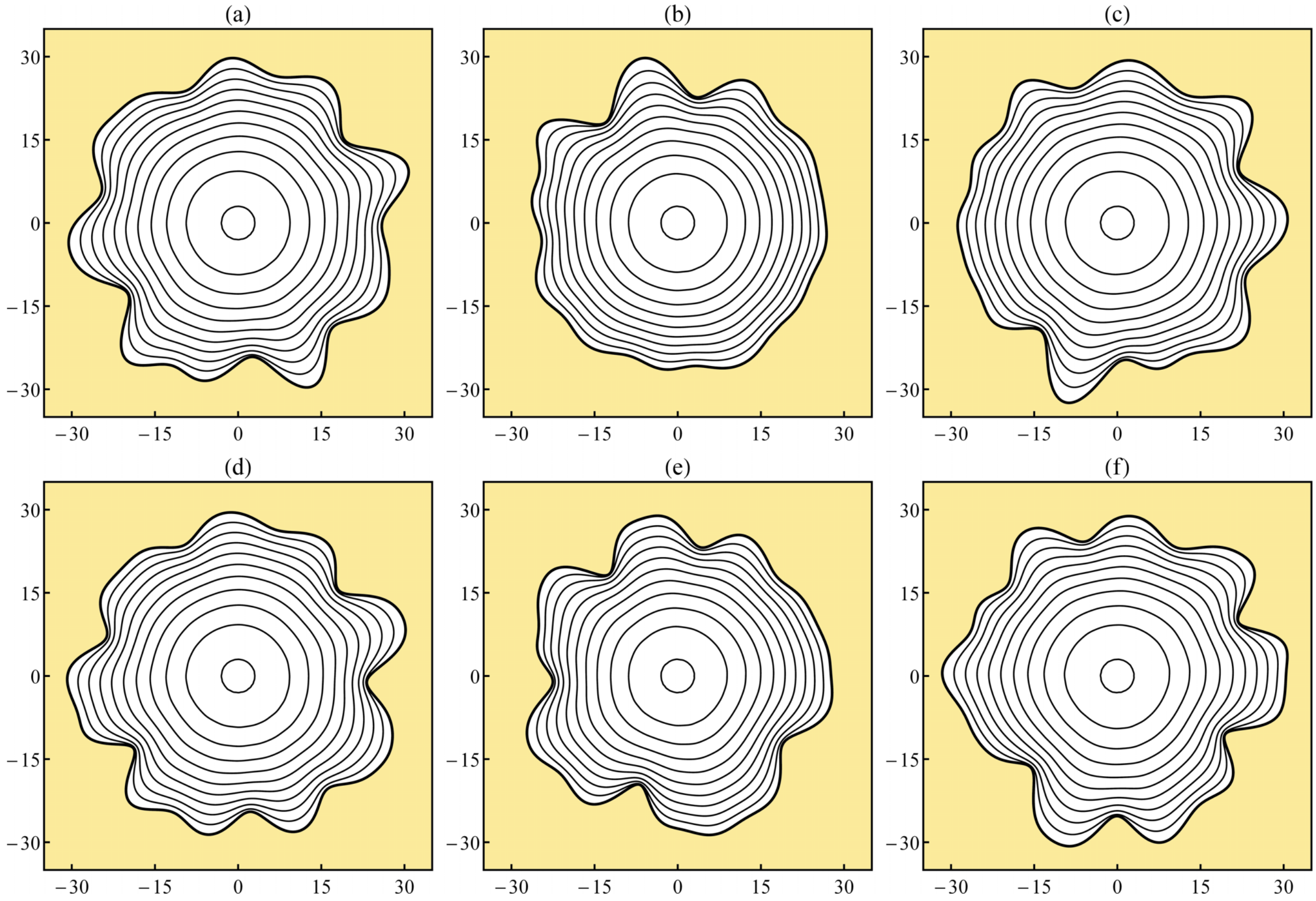

FIG. 6. Time evolution of the linear [(a)–(c)] and weakly nonlinear [(d)–(f)] interfacial patterns for $1 \leqslant n \leqslant 25$, $0 \leqslant t \leqslant t_f$, and equal time intervals $\Delta t = t_f/10$. The patterns are obtained for Bq = 30. Moreover, the values of t_f are (a) 2462, (b) 2199, (c) 2435, (d) 2423, (e) 2210, and (f) 2461. The sets of random phases utilized here are equal to those used in Fig. 5: Set I for (a) and (d), set II for (b) and (e), and set III for (c) and (f). The rest of the physical parameters are the same as the ones employed in Fig. 5. By comparing the linear [(a)–(c)] with the corresponding weakly nonlinear [(d)–(f)] structures, it is apparent that the nonlinear fingers are typically wider, having a greater tendency to split at their tips due to the action of surface rheological stresses.

II in (b) and (e), while set III is employed in (c) and (f). For each set of phases, the two resulting interfaces (linear and weakly nonlinear) are plotted one below the other to facilitate comparison between the patterns obtained by using the linear and weakly nonlinear approaches. In addition, the values of final times t_f in Fig. 6 are (a) 2462, (b) 2199, (c) 2435, (d) 2423, (e) 2210, and (f) 2461.

By inspecting the linear patterns depicted in Figs. 6(a)–6(c), one observes that despite the fact that the largest Boussinesq number used in Fig. 5 has been utilized (Bq = 30), the spreading of the fingers and the splitting of their tips are not clearly shown. As a matter of fact, regardless of the action of interfacial rheology effects, most of the fingers generated by purely linear theory are commonly narrow, and sharp at their tips. On the other hand, by examining the corresponding weakly nonlinear patterns presented in Figs. 6(d)–6(f), one can see that the nonlinear evolutions lead to the formation of wider fingers for which their tips become more blunt as time progresses. Indeed, these weakly nonlinear fingers spread, and some of them start to bifurcate, by splitting at the tips. These remarks indicate that a purely linear theory is not able to properly describe the basic, intrinsically nonlinear phenomena of finger tip widening and finger tip splitting involved in the pattern-forming process under the presence of interfacial rheological effects. All these findings reinforce the necessity and importance of developing a second-order weakly nonlinear theory for this physical system.

IV. CONCLUDING REMARKS

In this paper, we have investigated the effects of interfacial rheology on the morphology of the fingered structures that arise in radial Hele-Shaw cell flows during the early nonlinear stages of the dynamics. To tackle this nonlinear pattern formation problem, we used the Boussinesq-Scriven model and derived a generalized Young-Laplace pressure jump boundary condition for this Hele-Shaw flow, taking into account the effects of surface rheological stresses. Our derivation of such a key boundary condition generalizes a previous version originally calculated in Ref. [50] [their Eq. (10)] which assumed that the unit normal to the fluid-fluid interface pointed only in the radial direction and that the radial components of the fluid's velocities were continuous at the interface. Differently from what has been done in Ref. [50], we considered that the unit normal at the perturbed interface points in an arbitrary direction (i.e., a unit normal having both radial and azimuthal components). In this scenario, we considered a flow setup a little more general than the one considered in Ref. [50]. This has been done by expressing the velocity of the two-dimensional fluid that describes the interface approximately as the average of the inner and outer fluid velocities evaluated at the interface.

With the aforementioned generalized pressure difference boundary condition in hand, we performed a second extension of the work by Li and Manikantan: In Ref. [50], they employed a purely linear analysis of the problem, focusing on the stability of the fluid-fluid interface against small perturbations. On the contrary, in this paper we carried out a perturbative, second-order mode-coupling approach and concentrated our attention on examining how interfacial rheology effects influence the morphology and early nonlinear dynamics of the emerging fingered patterns. This is an important step, since one must go beyond linear (first-order) analysis to properly capture the most important, intrinsically nonlinear morphological aspects of the radial viscous fingering patterns. In this framework, and utilizing Darcy's law, we derived nonlinear, coupled differential equations that describe the time evolution of the interfacial perturbation amplitudes accurate to second order. Our weakly nonlinear results show that surface rheological stresses exert a dual role on the time evolution of the interface. On one hand, they tend to hinder the overall growth of the interface and delay the formation of interfacial disturbances. On the other hand, we have also found that increasing interfacial rheology effects favor finger tip-widening phenomena, enhancing the occurrence and intensity of the iconic finger tip-splitting events in radial Hele-Shaw flows.

Despite the progress achieved in this paper and in Ref. [50], many challenges still need to be addressed. A first theoretical improvement for future, more complete modeling would probably be to include the effects of interfacial surface tension gradients or Marangoni stresses. Other possible theoretical refinement would be to analyze an even more complex, structured interface and explore the influence of variable surface viscosity (non-Newtonian) effects on the nonlinear pattern-forming behavior of the system. An additional and certainly welcome advancement would be the development of numerical simulations that could allow checking the linear and weakly nonlinear predictions presented here and in Ref. [50], as well as to unveil still-unexplored pattern formation behaviors at fully nonlinear stages of the interfacial dynamics.

ACKNOWLEDGMENTS

J.A.M. thanks CNPq (Conselho Nacional de Desenvolvimento Científico e Tecnológico) for financial support under Grant No. 305140/2019-1. E.O.D. acknowledges financial support from CNPq (Conselho Nacional de Desenvolvimento Científico e Tecnológico) through Program No. 09/2020 (Grant No. 315759/2020-8) and Fundação de Amparo Ciência e Tecnologia do Estado de Pernambuco (FACEPE) through PPP Project No. APQ-0800-1.05/14. We are indebted to H. Manikantan and I. M. Coutinho for useful discussions and valuable suggestions.

APPENDIX A: USEFUL DERIVATIVES IN POLAR COORDINATES

In all the following equations, we consider that the unit normal vector to the perturbed interface may point in an arbitrary direction, having both radial and azimuthal components, i.e., $\mathbf{n} = n_r \hat{\mathbf{e}}_r + n_\theta \hat{\mathbf{e}}_\theta$:

$$\nabla = \hat{\mathbf{e}}_r \frac{\partial}{\partial r} + \hat{\mathbf{e}}_\theta \frac{1}{r}\frac{\partial}{\partial \theta}, \tag{A1}$$

$$\nabla_s = \hat{\mathbf{e}}_r n_\theta \left(n_\theta \frac{\partial}{\partial r} - \frac{n_r}{r}\frac{\partial}{\partial \theta} \right) + \hat{\mathbf{e}}_\theta n_r \left(\frac{n_r}{r}\frac{\partial}{\partial \theta} - n_\theta \frac{\partial}{\partial r} \right), \tag{A2}$$

$$\begin{aligned}\nabla \mathbf{u} = {} & \frac{\partial u_r}{\partial r}\hat{\mathbf{e}}_r\hat{\mathbf{e}}_r + \frac{\partial u_\theta}{\partial r}\hat{\mathbf{e}}_r\hat{\mathbf{e}}_\theta + \left(\frac{1}{r}\frac{\partial u_r}{\partial \theta} - \frac{u_\theta}{r} \right)\hat{\mathbf{e}}_\theta\hat{\mathbf{e}}_r \\ & + \left(\frac{1}{r}\frac{\partial u_\theta}{\partial \theta} + \frac{u_r}{r} \right)\hat{\mathbf{e}}_\theta\hat{\mathbf{e}}_\theta, \end{aligned} \tag{A3}$$

$$\begin{aligned}\nabla \mathbf{n} = {} & \frac{\partial n_r}{\partial r}\hat{\mathbf{e}}_r\hat{\mathbf{e}}_r + \frac{\partial n_\theta}{\partial r}\hat{\mathbf{e}}_r\hat{\mathbf{e}}_\theta + \left(\frac{1}{r}\frac{\partial n_r}{\partial \theta} - \frac{n_\theta}{r} \right)\hat{\mathbf{e}}_\theta\hat{\mathbf{e}}_r \\ & + \left(\frac{1}{r}\frac{\partial n_\theta}{\partial \theta} + \frac{n_r}{r} \right)\hat{\mathbf{e}}_\theta\hat{\mathbf{e}}_\theta, \end{aligned} \tag{A4}$$

$$\nabla \cdot \mathbf{u} = \frac{\partial u_r}{\partial r} + \frac{1}{r}\frac{\partial u_\theta}{\partial \theta} + \frac{u_r}{r}, \tag{A5}$$

$$\nabla \cdot \mathbf{n} = \frac{\partial n_r}{\partial r} + \frac{1}{r}\frac{\partial n_\theta}{\partial \theta} + \frac{n_r}{r}, \tag{A6}$$

$$\begin{aligned}\nabla_s \mathbf{u} = {} & \left(n_\theta^2 \frac{\partial u_r}{\partial r} - \frac{n_r n_\theta}{r}\frac{\partial u_r}{\partial \theta} + \frac{n_r n_\theta}{r} u_\theta \right)\hat{\mathbf{e}}_r\hat{\mathbf{e}}_r \\ & + \left(n_\theta^2 \frac{\partial u_\theta}{\partial r} - \frac{n_r n_\theta}{r}\frac{\partial u_\theta}{\partial \theta} - \frac{n_r n_\theta}{r} u_r \right)\hat{\mathbf{e}}_r\hat{\mathbf{e}}_\theta \\ & + \left(\frac{n_r^2}{r}\frac{\partial u_r}{\partial \theta} - \frac{n_r^2}{r} u_\theta - n_r n_\theta \frac{\partial u_r}{\partial r} \right)\hat{\mathbf{e}}_\theta\hat{\mathbf{e}}_r \\ & + \left(\frac{n_r^2}{r}\frac{\partial u_\theta}{\partial \theta} + \frac{n_r^2}{r} u_r - n_r n_\theta \frac{\partial u_\theta}{\partial r} \right)\hat{\mathbf{e}}_\theta\hat{\mathbf{e}}_\theta, \end{aligned} \tag{A7}$$

$$\begin{aligned}\nabla_s \mathbf{n} = {} & \left(n_\theta^2 \frac{\partial n_r}{\partial r} - \frac{n_r n_\theta}{r}\frac{\partial n_r}{\partial \theta} + \frac{n_r n_\theta^2}{r} \right)\hat{\mathbf{e}}_r\hat{\mathbf{e}}_r \\ & + \left(n_\theta^2 \frac{\partial n_\theta}{\partial r} - \frac{n_r n_\theta}{r}\frac{\partial n_\theta}{\partial \theta} - \frac{n_r^2 n_\theta}{r} \right)\hat{\mathbf{e}}_r\hat{\mathbf{e}}_\theta \\ & + \left(\frac{n_r^2}{r}\frac{\partial n_r}{\partial \theta} - \frac{n_r^2 n_\theta}{r} - n_r n_\theta \frac{\partial n_r}{\partial r} \right)\hat{\mathbf{e}}_\theta\hat{\mathbf{e}}_r \\ & + \left(\frac{n_r^2}{r}\frac{\partial n_\theta}{\partial \theta} + \frac{n_r^3}{r} - n_r n_\theta \frac{\partial n_\theta}{\partial r} \right)\hat{\mathbf{e}}_\theta\hat{\mathbf{e}}_\theta, \end{aligned} \tag{A8}$$

$$\begin{aligned}\nabla_s \cdot \mathbf{u} = {} & n_\theta^2 \frac{\partial u_r}{\partial r} + \frac{n_r^2}{r}\frac{\partial u_\theta}{\partial \theta} + \frac{n_r^2 u_r}{r} + \frac{1}{r} n_r n_\theta u_\theta \\ & - n_r n_\theta \left(\frac{\partial u_\theta}{\partial r} + \frac{1}{r}\frac{\partial u_r}{\partial \theta} \right), \end{aligned} \tag{A9}$$

and

$$\nabla_s \cdot \mathbf{n} = n_\theta^2 \frac{\partial n_r}{\partial r} + \frac{n_r^2}{r}\frac{\partial n_\theta}{\partial \theta} + \frac{n_r}{r} - n_r n_\theta \left(\frac{\partial n_\theta}{\partial r} + \frac{1}{r}\frac{\partial n_r}{\partial \theta} \right). \tag{A10}$$

Taking $\mathbf{u}=-\nabla\phi$, $n_r=1$, and $n_\theta=0$ in all these equations [(A1)–(A10)], we recover the equations of Appendix A of Ref. [50].

APPENDIX B: DERIVATION OF THE INTERFACIAL RHEOLOGY CONTRIBUTION TO THE GENERALIZED PRESSURE BOUNDARY CONDITION—EQ. (20)

In this Appendix, we derive the relation

$$\{\nabla_s\cdot[\nabla_s\mathbf{u}\cdot\mathbf{I}_s+\mathbf{I}_s\cdot(\nabla_s\mathbf{u})^T]\}\cdot\mathbf{n}=-2(\nabla_s\cdot\mathbf{u})\mathcal{K},\tag{B1}$$

which arises in the passage from Eq. (10) to Eq. (11) with η_s being a constant. We begin writing $\mathbf{I}_s$ in its matrix representation:

$$\mathbf{I}_s=\begin{pmatrix}1&0\\0&1\end{pmatrix}-\begin{pmatrix}n_r\\n_\theta\end{pmatrix}\begin{pmatrix}n_r&n_\theta\end{pmatrix}=\begin{pmatrix}n_\theta^2&-n_rn_\theta\\-n_rn_\theta&n_r^2\end{pmatrix}.\tag{B2}$$

From Eq. (B2), we express the left-hand side of Eq (B1) as $(\nabla_s\cdot\boldsymbol{\Gamma})\cdot\mathbf{n}$, where

$$\boldsymbol{\Gamma}=[\nabla_s\mathbf{u}\cdot\mathbf{I}_s+\mathbf{I}_s\cdot(\nabla_s\mathbf{u})^T]=\begin{pmatrix}\Gamma_{rr}&\Gamma_{r\theta}\\\Gamma_{\theta r}&\Gamma_{\theta\theta}\end{pmatrix},\tag{B3}$$

with $\Gamma_{r\theta}=\Gamma_{\theta r}$. Using Eq. (A2), we have

$$\nabla_s\cdot\boldsymbol{\Gamma}=\left[\hat{\mathbf{e}}_r\cdot\left(n_\theta^2\frac{\partial}{\partial r}-\frac{n_rn_\theta}{r}\frac{\partial}{\partial\theta}\right)+\hat{\mathbf{e}}_\theta\cdot\left(\frac{n_r^2}{r}\frac{\partial}{\partial\theta}-n_rn_\theta\frac{\partial}{\partial r}\right)\right][\Gamma_{rr}\mathbf{e}_r\mathbf{e}_r+\Gamma_{r\theta}(\mathbf{e}_r\mathbf{e}_\theta+\mathbf{e}_\theta\mathbf{e}_r)+\Gamma_{\theta\theta}\mathbf{e}_\theta\mathbf{e}_\theta].\tag{B4}$$

The computation of the RHS of Eq. (B4) requires the relations

$$\begin{aligned}&\partial_\theta(\mathbf{e}_r\mathbf{e}_r)=\mathbf{e}_\theta\mathbf{e}_r+\mathbf{e}_r\mathbf{e}_\theta,\ \partial_\theta(\mathbf{e}_r\mathbf{e}_\theta)=\mathbf{e}_\theta\mathbf{e}_\theta-\mathbf{e}_r\mathbf{e}_r,\\&\partial_\theta(\mathbf{e}_\theta\mathbf{e}_r)=-\mathbf{e}_r\mathbf{e}_r+\mathbf{e}_\theta\mathbf{e}_\theta,\ \partial_\theta(\mathbf{e}_\theta\mathbf{e}_\theta)=-\mathbf{e}_r\mathbf{e}_\theta-\mathbf{e}_\theta\mathbf{e}_r,\end{aligned}\tag{B5}$$

and $\partial_r(\mathbf{e}_i\mathbf{e}_j)=0$, with $i,j=r,\theta$. Thus, Eq. (B4) becomes

$$\begin{aligned}\nabla_s\cdot\boldsymbol{\Gamma}=&\left[n_\theta^2\frac{\partial\Gamma_{rr}}{\partial r}+\frac{n_rn_\theta}{r}\left(2\Gamma_{r\theta}-\frac{\partial\Gamma_{rr}}{\partial\theta}\right)+\frac{n_r^2}{r}\left(\frac{\partial\Gamma_{r\theta}}{\partial\theta}+\Gamma_{rr}-\Gamma_{\theta\theta}\right)-n_rn_\theta\frac{\partial\Gamma_{r\theta}}{\partial r}\right]\mathbf{e}_r\\&+\left[n_\theta^2\frac{\partial\Gamma_{r\theta}}{\partial r}+\frac{n_rn_\theta}{r}\left(\Gamma_{\theta\theta}-\Gamma_{rr}-\frac{\partial\Gamma_{r\theta}}{\partial\theta}\right)+\frac{n_r^2}{r}\left(\frac{\partial\Gamma_{\theta\theta}}{\partial\theta}+2\Gamma_{r\theta}\right)-n_rn_\theta\frac{\partial\Gamma_{\theta\theta}}{\partial r}\right]\mathbf{e}_\theta,\end{aligned}\tag{B6}$$

and the contraction of this equation with the unit normal vector $\mathbf{n}$ can be written as

$$\begin{aligned}(\nabla_s\cdot\boldsymbol{\Gamma})\cdot\mathbf{n}=&\,n_rn_\theta^2\frac{\partial}{\partial r}(\Gamma_{rr}-\Gamma_{\theta\theta})+n_\theta\left(n_\theta^2-n_r^2\right)\frac{\partial\Gamma_{r\theta}}{\partial r}+\frac{n_\theta n_r^2}{r}\left[4\Gamma_{r\theta}-\frac{\partial}{\partial\theta}(\Gamma_{rr}-\Gamma_{\theta\theta})\right]\\&+\frac{n_r\left(n_r^2-n_\theta^2\right)}{r}\left[(\Gamma_{rr}-\Gamma_{\theta\theta})+\frac{\partial\Gamma_{r\theta}}{\partial\theta}\right].\end{aligned}\tag{B7}$$

Note that the expression above depends only on $\Gamma_{r\theta}$ and the difference $\Gamma_{rr}-\Gamma_{\theta\theta}$. Now, calculating the components of $\boldsymbol{\Gamma}$ using Appendix A, we have

$$\begin{aligned}\Gamma_{rr}&=(\nabla_s\mathbf{u})_{rr}(\mathbf{I}_s)_{rr}+(\nabla_s\mathbf{u})_{r\theta}(\mathbf{I}_s)_{\theta r}+(\mathbf{I}_s)_{rr}[(\nabla_s\mathbf{u})^T]_{rr}+(\mathbf{I}_s)_{r\theta}[(\nabla_s\mathbf{u})^T]_{\theta r}\\&=2\left[\left(n_\theta^2\frac{\partial u_r}{\partial r}-\frac{n_rn_\theta}{r}\frac{\partial u_r}{\partial\theta}+\frac{n_rn_\theta}{r}u_\theta\right)n_\theta^2-n_rn_\theta\left(n_\theta^2\frac{\partial u_\theta}{\partial r}-\frac{n_rn_\theta}{r}\frac{\partial u_\theta}{\partial\theta}-\frac{n_rn_\theta}{r}u_r\right)\right]\\&=2n_\theta^2\left[n_\theta^2\frac{\partial u_r}{\partial r}+n_r^2\left(\frac{1}{r}\frac{\partial u_\theta}{\partial\theta}+\frac{1}{r}u_r\right)+n_rn_\theta\left(\frac{1}{r}u_\theta-\frac{1}{r}\frac{\partial u_r}{\partial\theta}-\frac{\partial u_\theta}{\partial r}\right)\right]=2n_\theta^2(\nabla_s\cdot\mathbf{u}),\end{aligned}\tag{B8}$$

$$\begin{aligned}\Gamma_{\theta\theta}&=2[(\nabla_s\mathbf{u})_{\theta\theta}(\mathbf{I}_s)_{\theta\theta}+(\nabla_s\mathbf{u})_{\theta r}(\mathbf{I}_s)_{r\theta}]\\&=2\left[\left(\frac{n_r^2}{r}\frac{\partial u_\theta}{\partial\theta}+\frac{n_r^2}{r}u_r-n_rn_\theta\frac{\partial u_\theta}{\partial r}\right)n_r^2-n_rn_\theta\left(\frac{n_r^2}{r}\frac{\partial u_r}{\partial\theta}-\frac{n_r^2}{r}u_\theta-n_rn_\theta\frac{\partial u_r}{\partial r}\right)\right]\\&=2n_r^2\left[n_\theta^2\frac{\partial u_r}{\partial r}+n_r^2\left(\frac{1}{r}\frac{\partial u_\theta}{\partial\theta}+\frac{1}{r}u_r\right)+n_rn_\theta\left(\frac{1}{r}u_\theta-\frac{1}{r}\frac{\partial u_r}{\partial\theta}-\frac{\partial u_\theta}{\partial r}\right)\right]=2n_r^2(\nabla_s\cdot\mathbf{u}),\end{aligned}\tag{B9}$$

and

$$\begin{aligned}\Gamma_{r\theta}&=(\nabla_s\mathbf{u})_{rr}(\mathbf{I}_s)_{r\theta}+(\nabla_s\mathbf{u})_{r\theta}(\mathbf{I}_s)_{\theta\theta}+(\mathbf{I}_s)_{rr}[(\nabla_s\mathbf{u})^T]_{r\theta}+(\mathbf{I}_s)_{r\theta}[(\nabla_s\mathbf{u})^T]_{\theta\theta}\\&=(\mathbf{I}_s)_{r\theta}(\nabla_s\cdot\mathbf{u})+n_r^2\left(n_\theta^2\frac{\partial u_\theta}{\partial r}-\frac{n_rn_\theta}{r}\frac{\partial u_\theta}{\partial\theta}-\frac{n_rn_\theta}{r}u_r\right)+n_\theta^2\left(\frac{n_r^2}{r}\frac{\partial u_r}{\partial\theta}-\frac{n_r^2}{r}u_\theta-n_rn_\theta\frac{\partial u_r}{\partial r}\right)\\&=-n_rn_\theta\left[(\nabla_s\cdot\mathbf{u})+n_\theta^2\frac{\partial u_r}{\partial r}+n_r^2\left(\frac{1}{r}u_r+\frac{1}{r}\frac{\partial u_\theta}{\partial\theta}\right)+n_rn_\theta\left(\frac{1}{r}u_\theta-\frac{1}{r}\frac{\partial u_r}{\partial\theta}-\frac{\partial u_\theta}{\partial r}\right)\right]=-2n_rn_\theta(\nabla_s\cdot\mathbf{u}).\end{aligned}\tag{B10}$$

By inspecting Eqs. (B8)–(B10), we observe that

$$\Gamma_{r\theta} = \frac{n_r n_\theta}{n_r^2 - n_\theta^2}(\Gamma_{rr} - \Gamma_{\theta\theta}). \tag{B11}$$

Substituting this relation into Eq. (B7), we obtain

$$(\boldsymbol{\nabla}_s \cdot \boldsymbol{\Gamma}) \cdot \mathbf{n} = \left[n_\theta^2 \frac{\partial n_r}{\partial r} + \frac{n_r^2}{r}\frac{\partial n_\theta}{\partial \theta} + \frac{n_r}{r} - n_r n_\theta\left(\frac{\partial n_\theta}{\partial r} + \frac{1}{r}\frac{\partial n_r}{\partial \theta}\right)\right]\frac{\Gamma_{rr} - \Gamma_{\theta\theta}}{n_r^2 - n_\theta^2}. \tag{B12}$$

To derive the relation (B1) from Eq. (B12), first notice that by using Eqs. (B8) and (B9), the difference $\Gamma_{rr} - \Gamma_{\theta\theta}$ in Eq. (B12) can be written as

$$\Gamma_{rr} - \Gamma_{\theta\theta} = -2\big(n_r^2 - n_\theta^2\big)(\boldsymbol{\nabla}_s \cdot \mathbf{u}). \tag{B13}$$

Besides, from Eq. (A10), we notice that the expression in the brackets of Eq. (B12) is equal to $\boldsymbol{\nabla}_s \cdot \mathbf{n}$. Finally, plugging $\boldsymbol{\nabla}_s \cdot \mathbf{n}$ and Eq. (B13) into Eq. (B12), we obtain the relation (B1):

$$\begin{aligned}(\boldsymbol{\nabla}_s \cdot \boldsymbol{\Gamma}) \cdot \mathbf{n} &= \{\boldsymbol{\nabla}_s \cdot [\boldsymbol{\nabla}_s \mathbf{u} \cdot \mathbf{I}_s + \mathbf{I}_s \cdot (\boldsymbol{\nabla}_s \mathbf{u})^T]\} \cdot \mathbf{n}\\ &= -2(\boldsymbol{\nabla}_s \cdot \mathbf{n})(\boldsymbol{\nabla}_s \cdot \mathbf{u}).\end{aligned} \tag{B14}$$

APPENDIX C: EXPRESSIONS FOR THE NONLINEAR MODE-COUPLING FUNCTIONS

In this Appendix, we present the expressions of the nonlinear mode-coupling functions of Eq. (28), F, F_R, F_S, G, G_S, and G_R:

$$\begin{aligned}F(n, n') = \frac{1}{s(n)}\Bigg\{&\frac{A|n|}{2\pi R^3}\left[\frac{1}{2} - \mathrm{sgn}(nn')\right]\\ &- \frac{(A+1)|n|}{2\mathrm{Ca}R^4}\left[1 - \frac{n'}{2}(3n' + n)\right]\Bigg\},\end{aligned} \tag{C1}$$

$$\begin{aligned}F_S(n, n') = \frac{|n|}{12\pi R^5 s(n)}&[|n'| + n\,\mathrm{sgn}(n')\\ &- A(n|n|\,\mathrm{sgn}(n') - n'^2 + 1)],\end{aligned} \tag{C2}$$

$$\begin{aligned}F_R(n, n') = -&\frac{\mathrm{Bq}(A+1)|n|}{48\pi R^6 s(n)}\\ &\times\left\{3 + n^2[1 + \mathrm{sgn}(nn')] - \frac{7}{2}n'^2 - \frac{5}{2}nn'\right\},\end{aligned} \tag{C3}$$

$$G(n, n') = \frac{1}{Rs(n)}\{A|n|[1 - \mathrm{sgn}(nn')] - 1\}, \tag{C4}$$

$$\begin{aligned}G_S(n, n') = \frac{|n|}{6R^3 s(n)}&\{n\,\mathrm{sgn}(n') + |n'| - |n|\\ &- A[n|n|\,\mathrm{sgn}(n') - 2nn' + n'^2 - 1]\},\end{aligned} \tag{C5}$$

and

$$\begin{aligned}G_R(n, n') = -\frac{\mathrm{Bq}(A+1)|n|}{24R^4 s(n)}&\{n^2[1 + \mathrm{sgn}(nn')] - 2\\ &+ 2n'^2 - 4nn'\}.\end{aligned} \tag{C6}$$

Note that the sgn function equals ±1 according to the sign of its argument.

---

[1] For review articles on the viscous fingering instability see, for example, G. M. Homsy, Viscous fingering in porous media, Annu. Rev. Fluid Mech. **19**, 271 (1987); K. V. McCloud and J. V. Maher, Experimental perturbations to Saffman-Taylor flow, Phys. Rep. **260**, 139 (1995); J. Casademunt, Viscous fingering as a paradigm of interfacial pattern formation: Recent results and new challenges, Chaos **14**, 809 (2004).

[2] P. G. Saffman and G. I. Taylor, The penetration of a fluid into a porous medium or Hele-Shaw cell containing a more viscous liquid, Proc. R. Soc. London A **245**, 312 (1958).

[3] G. Tryggvason and H. Aref, Numerical experiments on Hele-Shaw flow with a sharp interface, J. Fluid Mech. **136**, 1 (1983).

[4] J. V. Maher, Development of Viscous Fingering Patterns, Phys. Rev. Lett. **54**, 1498 (1985).

[5] T. Maxworthy, The nonlinear growth of a gravitationally unstable interface in a Hele-Shaw cell, J. Fluid Mech. **177**, 207 (1987).

[6] J. A. Miranda and M. Widom, Weakly nonlinear investigation of the Saffman-Taylor problem in a rectangular Hele-Shaw cell, Int. J. Mod. Phys. B **12**, 931 (1998).

[7] L. Paterson, Radial fingering in a Hele-Shaw cell, J. Fluid Mech. **113**, 513 (1981).

[8] J. D. Chen, Growth of radial viscous fingers in a Hele-Shaw cell, J. Fluid Mech. **201**, 223 (1989).

[9] J. A. Miranda and M. Widom, Radial fingering in a Hele-Shaw cell: A weakly nonlinear analysis, Physica D **120**, 315 (1998).

[10] E. Lajeunesse and Y. Couder, On tip splitting instability of viscous fingers, J. Fluid Mech. **419**, 125 (2000).

[11] I. Bischofberger, R. Ramanchandran, and S. R. Nagel, An island of stability in a sea of fingers: Emergent global features of the viscous-flow instability, Soft Matter **11**, 7428 (2015).

[12] J. Sheng, *Modern Chemical Enhanced Oil Recovery: Theory and Practice* (Gulf Professional Publishing, Boston, 2010).

[13] A. W. Woods, *Flow in Porous Rocks* (Cambridge University Press, Cambridge, 2015).

[14] B. Metz, O. Davidson, H. De Connick, M. Loos, and L. Meyer, *IPCC Special Report on Carbon Dioxide Capture and Storage* (Cambridge University Press, New York, 2005).

[15] E. Ben-Jacob and P. Garik, The formation of patterns in nonequilibrium growth, Nature (London) **343**, 523 (1990).

[16] B. Jha, L. Cueto-Felgueroso, and R. Juanes, Fluid Mixing from Viscous Fingering, Phys. Rev. Lett. **106**, 194502 (2011).

[17] H.-Y. Chu and H.-K. Lee, Evolution of the Plasma Bubble in a Narrow Gap, Phys. Rev. Lett. **107**, 225001 (2011).

[18] C. Blanch-Mercader and J. Casademunt, Spontaneous Motility of Actin Lamellar Fragments, Phys. Rev. Lett. **110**, 078102 (2013).

[19] L. Kondic, M. J. Shelley, and P. Palffy-Muhoray, Non-Newtonian Hele-Shaw Flow and the Saffman-Taylor Instability, Phys. Rev. Lett. **80**, 1433 (1998).

[20] A. Eslami and S. M. Taghavi, Viscous fingering regimes in elasto-visco-plastic fluids, J. Non-Newtonian Fluid Mech. **243**, 79 (2017).

[21] C.-Y. Chen and E. Meiburg, Miscible porous media displacements in the quarter five-spot configuration. Part 1. The homogeneous case, J. Fluid Mech. **371**, 233 (1998).

[22] V. Sharma, S. Nand, S. Pramanik, C.-Y. Chen, and M. Mishra, Control of radial miscible viscous fingering, J. Fluid Mech. **884**, A16 (2020).

[23] R. X. Suzuki, Y. Nagatsu, M. Mishra, and T. Ban, Phase separation effects on a partially miscible viscous fingering dynamics, J. Fluid Mech. **898**, A11 (2020).

[24] T. Podgorski, M. C. Sostarecz, S. Zorman, and A. Belmonte, Fingering instabilities of a reactive micellar interface, Phys. Rev. E **76**, 016202 (2007).

[25] Y. Nagatsu, Viscous fingering phenomena with chemical reactions, Curr. Phys. Chem. **5**, 52 (2015).

[26] D. P. Jackson, R. E. Goldstein, and A. O. Cebers, Hydrodynamics of fingering instabilities in dipolar fluids, Phys. Rev. E **50**, 298 (1994).

[27] C. Flament, G. Pacitto, J.-C. Bacri, I. Drikis, and A. Cebers, Viscous fingering in a magnetic fluid. I. RadialHele-Shaw flow, Phys. Fluids **10**, 2464 (1998).

[28] T. Gao, M. Mirzadeh, P. Bai, K. Conforti, and M. Bazant, Active control of viscous fingering using electric fields, Nat. Commun. **10**, 4002 (2019).

[29] P. H. A. Anjos, M. Zhao, J. Lowengrub, and S. Li, Electrically controlled self-similar evolution of viscous fingering patterns, Phys. Rev. Fluids **7**, 053903 (2022).

[30] S. W. Li, J. S. Lowengrub, J. Fontana, and P. Palffy-Muhoray, Control of Viscous Fingering Patterns in a Radial Hele-Shaw Cell, Phys. Rev. Lett. **102**, 174501 (2009).

[31] E. O. Dias, E. Alvarez-Lacalle, M. S. Carvalho, and J. A. Miranda, Minimization of Viscous Fluid Fingering: A Variational Scheme for Optimal Flow Rates, Phys. Rev. Lett. **109**, 144502 (2012).

[32] L. C. Morrow, T. J. Moroney, and S. W. McCue, Numerical investigation of controlling interfacial instabilities in non-standard Hele-Shaw configurations, J. Fluid Mech. **877**, 1063 (2019).

[33] R. Arun, S. T. M. Dawson, P. J. Schmid, A. Laskari, and B. J. McKeon, Control of instability by injection rate oscillations in a radial Hele-Shaw cell, Phys. Rev. Fluids **5**, 123902 (2020).

[34] P. H. A. Anjos, M. Zhao, J. Lowengrub, and S. Li, Electrically-controlled self-similar evolution of viscous fingering patterns in radial Hele-Shaw flows, arXiv:2111.03102.

[35] J. Kim, F. Xu, S. Lee, Formation and Destabilization of the Particle Band on the Fluid-Fluid Interface, Phys. Rev. Lett. **118**, 074501 (2017).

[36] R. Luo, Y. Chen, and S. Lee, Particle-induced viscous fingering: Review and outlook, Phys. Rev. Fluids **3**, 110502 (2018).

[37] E. Alvarez-Lacalle, J. Ortín, and J. Casademunt, Low viscosity contrast fingering in a rotating Hele-Shaw cell, Phys. Fluids **16**, 908 (2004).

[38] C.-Y. Chen, Y.-S. Huang, and J. A. Miranda, Diffuse-interface approach to rotating Hele-Shaw flows, Phys. Rev. E **84**, 046302 (2011).

[39] C. W. Park and G. M. Homsy, Two-phase displacement in Hele Shaw cells: Theory, J. Fluid Mech. **139**, 291 (1984).

[40] S. J. Jackson, D. Stevens, D. Giddings, and H. Power, Dynamic-wetting effects in finite-mobility-ratio HeleShaw flow, Phys. Rev. E **92**, 023021 (2015).

[41] C. Ruyer-Quil, Inertial corrections to the Darcy law in a Hele-Shaw cell, C. R. Acad. Sci., Ser. IIb: Mec. **329**, 337 (2001).

[42] C. Chevalier, M. Ben Amar, D. Bonn, and A. Lindner, Inertial effects on Saffman-Taylor viscous fingering, J. Fluid Mech. **552**, 83 (2006).

[43] E. O. Dias and J. A. Miranda, Influence of inertia on viscous fingering patterns: Rectangular and radial flows, Phys. Rev. E **83**, 066312 (2011).

[44] H. Zhao and J. V. Maher, Viscous fingering experiments with periodic boundary conditions, Phys. Rev. A **42**, 5894 (1990).

[45] F. Parisio, F. Moraes, J. A. Miranda, and M. Widom, Saffman-Taylor problem on a sphere, Phys. Rev. E **63**, 036307 (2001).

[46] H. Zhao, J. Casademunt, C. Yeung, and J. V. Maher, Perturbing Hele-Shaw flow with a small gap gradient, Phys. Rev. A **45**, 2455 (1992).

[47] D. Pihler-Puzović, P. Illien, M. Heil, and A. Juel, Suppression of Complex Fingerlike Patterns at the Interface between Air and a Viscous Fluid by Elastic Membranes, Phys. Rev. Lett. **108**, 074502 (2012).

[48] T. T. Al-Housseiny and H. A. Stone, Controlling viscous fingering in tapered Hele-Shaw cells, Phys. Fluids **25**, 092102 (2013).

[49] G. Bongrand and P. A. Tsai, Manipulation of viscous fingering in a radially tapered cell geometry, Phys. Rev. E **97**, 061101(R) (2018).

[50] J. Li and H. Manikantan, Influence of interfacial rheology on viscous fingering, Phys. Rev. Fluids **6**, 074001 (2021).

[51] M. S. Bhamla, C. E. Giacomin, C. Balemans, and G. G. Fuller, Influence of interfacial rheology on drainage from curved surfaces, Soft Matter **10**, 6917 (2014).

[52] G. Lin, J. M. Frostad, and G. G. Fuller, Influence of interfacial elasticity on liquid entrainment in thin foam films, Phys. Rev. Fluids **3**, 114001 (2018).

[53] A. K. Sachan, S. Q. Choi, K. H. Kim, Q. Tang, L. Hwang, K. Y. C. Lee, T. M. Squires, and J. A. Zasadzinski, Interfacial rheology of coexisting solid and fluid monolayers, Soft Matter **13**, 1481 (2017).

[54] C. C. Chang, A. Nowbahar, V. Mansard, I. Williams, J. Mecca, A. K. Schmitt, T. H. Kalantar, T. C. Kuo, and T. M. Squires, Interfacial rheology and heterogeneity of aging asphaltene layers at the water-oil interface, Langmuir **34**, 5409 (2018).

[55] H. Manikantan and T. M. Squires, Surfactant dynamics: Hidden variables controlling fluid flows, J. Fluid Mech. **892**, P1 (2020).

[56] D. Langevin, Rheology of adsorbed surfactant monolayers at fluid surfaces, Annu. Rev. Fluid Mech. **46**, 47 (2014).

[57] Z. A. Zell, A. Nowbahar, V. Mansard, L. G. Leal, S. S. Deshmukh, J. M. Mecca, C. J. Tucker, and T. M. Squires,

Surface shear inviscidity of soluble surfactants, Proc. Natl. Acad. Sci. USA **111**, 3677 (2014).

[58] N. Jaensson and J. Vermant, Tensiometry and rheology of complex interfaces, Curr. Opin. Colloid Interface Sci. **37**, 136 (2018).

[59] G. G. Fuller and J. Vermant, Complex fluid-fluid interfaces: Rheology and structure, Annu. Rev. Chem. Biomol. Eng. **3**, 519 (2012).

[60] J. M. Boussinesq, On the existence of a surface viscosity, in the thin transition layer separating a liquid from another contiguous fluid, Ann. Chim. Phys. **29**, 349 (1913).

[61] L. E. Scriven, Dynamics of a fluid interface equation of motion for Newtonian surface fluids, Chem. Eng. Sci. **12**, 98 (1960).

[62] L. E. Scriven and C. V. Sternling, The Marangoni effects, Nature (London) **187**, 186 (1960).

[63] L. N. Brush, R. F. Sekerka, and G. B. McFadden, A numerical and analytical study of nonlinear bifurcations associated with the morphological stability of two-dimensional single crystals, J. Cryst. Growth **100**, 89 (1990).

[64] S. W. Haan, Weakly nonlinear hydrodynamic instabilities in inertial fusion, Physics of Fluids B: Plasma Physics **3**, 2349 (1991).

[65] H. Guo, D. C. Hong, and D. A. Kurtze, Surface-Tension-Driven Nonlinear Instability in Viscous Fingers, Phys. Rev. Lett. **69**, 1520 (1992).

[66] H. Guo, D. C. Hong, and D. A. Kurtze, Dynamics of viscous fingers and threshold instability, Phys. Rev. E **51**, 4469 (1995).

[67] E. Alvarez-Lacalle, J. Casademunt, and J. Ortín, Systematic weakly nonlinear analysis of interfacial instabilities in Hele-Shaw flows, Phys. Rev. E **64**, 016302 (2001).

[68] E. Alvarez-Lacalle, E. Pauné, J. Casademunt, and J. Ortín, Systematic weakly nonlinear analysis of radial viscous fingering, Phys. Rev. E **68**, 026308 (2003).

[69] A. D. Dinsmore, M. F. Hsu, M. G. Nikolaides, M. Marquez, A. R. Bausch, and D. A. Weitz, Colloidosomes: Selectively permeable capsules composed of colloidal particles, Science **298**, 1006 (2002).

[70] H. Noguchi, and G. Gompper, Shape transitions of fluid vesicles and red blood cells in capillary flows, Proc. Natl. Acad. Sci. USA **102**, 14159 (2005).

[71] J. A. Zasadzinski, J. Ding, H. E. Warriner, F. Bringezu, and F, Waring, The physics and physiology of lung surfactants, Curr. Opin. Colloid Interface Sci. **6**, 506 (2001).

[72] K. J. Stebe and D. Barthès-Biesel, Marangoni effects of adsorption'desorption controlled surfactants on the leading end of an infinitely long bubble in a capillary, J. Fluid Mech. **286**, 25 (1995).

[73] J. C. Slattery, L. Sagis, and E.-S. Oh, *Interfacial Transport Phenomena*, 2nd ed. (Springer, Berlin, 2007).

[74] D. A. Edwards, H. Brenner, and D. T. Wasan, *Interfacial Transport Processes and Rheology* (Butterworth, MA, 1991).

[75] J. W. McLean and P. G. Saffman, J. Fluid Mech. **102**, 455 (1981); P. G Saffman, in *Macroscopic Properties of Disordered Media, Lecture Notes in Physics*, edited by R. Burridge, S. Childress and G. Papanicolaou (Springer-Verlag, New York, 1982), Vol. 154, p. 208.

[76] For a discussion on the influence of wall wetting effects on the curvature in the direction perpendicular to the plates, see Ref. [39] and D. A. Reinelt, J. Fluid Mech. **183**, 219 (1987).

[77] L. D. Landau and E. M. Lifshitz, *Course of Theoretical Mechanics: Fluid Mechanics* (Pergamon Press, New York, 1959), Vol. 6.

[78] R. L. Panton, *Incompressible Flow* (Wiley, Hoboken, 2013).

[79] G. K. Batchelor, *An Introduction to Fluid Dynamics* (Cambridge University Press, Cambridge, 1967).

[80] W. E. Langlois and M. O. Deville, *Slow Viscous Flow*, 2nd ed., (Springer, New York, 2014).

[81] Í. M. Coutinho, F. M. Rocha, and J. A. Miranda, Viscous normal stresses and fingertip tripling in radial Hele-Shaw flows, Phys. Rev. E **104**, 045106 (2021).

[82] H. Kim, T. Funada, D. D. Joseph, and G. M. Homsy, Viscous potential flow analysis of radial fingering in a Hele-Shaw cell, Phys. Fluids **21**, 074106 (2009).

[83] D. Georgieva, V. Schmitt, F. Leal-Calderon, and D. Langevin, On the possible role of surface elasticity in emulsion stability, Langmuir **25**, 5565 (2009).

[84] D. M. A. Buzza, C.-Y. D. Lu, and M. E. Cates, Linear shear rheology of incompressible foams, J. Phys. II **5**, 37 (1995).

[85] T. J. Stoodt and J. C. Slattery, Effect of the interfacial viscosities upon displacement, AIChE J. **30**, 564 (1984).

[86] J. A. Miranda and E. Alvarez-Lacalle, Viscosity contrast effects on fingering formation in rotating Hele-Shaw flows, Phys. Rev. E **72**, 026306 (2005).

[87] P. H. A. Anjos and S. Li, Weakly nonlinear analysis of the Saffman-Taylor problem in a radially spreading fluid annulus, Phys. Rev. Fluids **5**, 054002 (2020).

[88] M. Zhao, P. H. A. Anjos, J. Lowengrub, and S. Li, Pattern formation of the three-layer Saffman-Taylor problem in a radial Hele-Shaw cell, Phys. Rev. Fluids **5**, 124005 (2020).

[89] R. M. Oliveira and J. A. Miranda, Fully nonlinear simulations of ferrofluid patterns in a radial magnetic field, Phys. Rev. Fluids **5**, 124003 (2020).

[90] R. M. Oliveira, I. M. Coutinho, P. H. A. Anjos, and J. A. Miranda, Shape instabilities in confined ferrofluids under crossed magnetic fields, Phys. Rev. E **104**, 065113 (2021).

[91] M. J. P. Gingras and Z. Rácz, Noise and the linear stability analysis of viscous fingering, Phys. Rev. A **40**, 5960 (1989).

[92] E. O. Dias, and J. A. Miranda, Wavelength selection in Hele-Shaw flows: A maximum-amplitude criterion, Phys. Rev. E **88**, 013016 (2013).

[93] S. S. S. Cardoso and A. W. Woods, The formation of drops through viscous instability, J. Fluid Mech. **289**, 351 (1995).